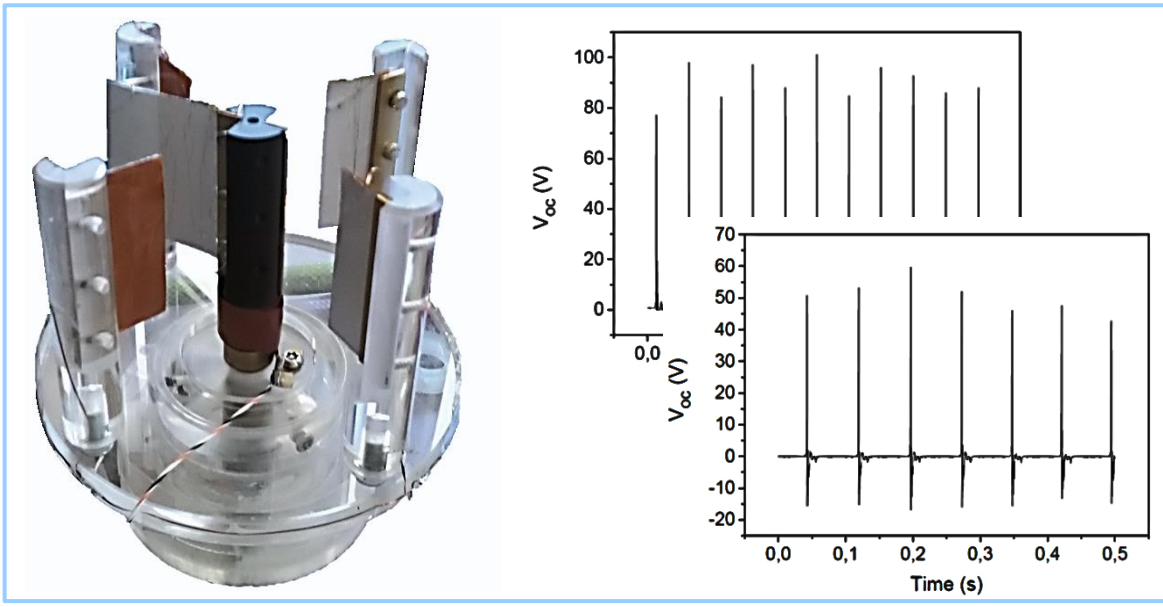

Scavenging Energy from The Motion of Fluids: Novel Nanogenerators Based on Triboelectricity

Cátia Raquel da Silva Rodrigues
Integrated Masters in Engineering Physics
Department of Physics and Astronomy
2015

Supervisor
Dr. João O. Ventura, Auxiliary Researcher, Faculty of Sciences of the University of Porto

Co-Supervisor
Dr. André M. Pereira, Auxiliar Professor and Auxiliary Researcher, Faculty of Sciences of the University of Porto

All modifications determined by the Jury, and only those, were made.

The president of the Jury:

Porto, _____/_____/_____

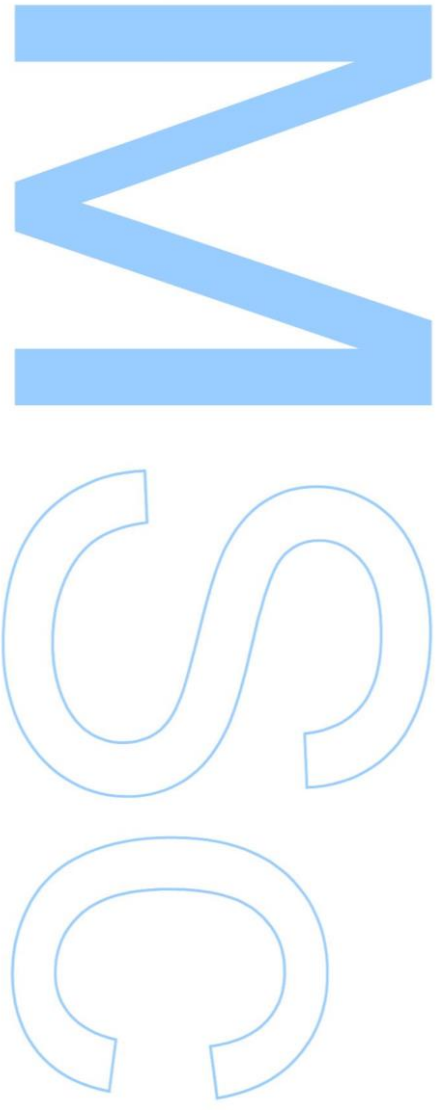

"To raise new questions, new possibilities, to regard old problems from a new angle, requires creative imagination and marks real advance in science."

Albert Einstein

Acknowledgements

As the author of this dissertation, I would like to recognize those who were most relevant in my personal and professional development and who are ultimately responsible for providing me with all the necessary tools to accomplish this dissertation.

First of all I have to thank my supervisors, Dr. João Ventura and Dr. André Pereira, I want to thank them for this great opportunity this project, for all words of motivation that often needed to continue my work and for all the opportunities they provided. I am grateful for trusting in me when I did not trust myself, for all the advices, debates and all the support whenever the work reached a dead end.

I have to thank Eng. Francisco Carpiteiro and Technician Fernando of the Department's Workshop, for all the help, time spent, patience and assistance in designing and development of device. Eng. Francisco Carpiteiro played an important role throughout this project through its expertise in implementing manufacture of mechanical parts of the device. I am also in debt to Eng. Pedro of the Department's Electronics Workshop for all the help with all electronic issues during this project. A big thank you to him for his availability and the knowledge of electronics who taught me. The patience and friendship of both Eng. Francisco and Eng. Pedro helped me through the setbacks.

For all the help, counsel, support and company during the work, I thank my colleagues and friends, Carla Alves, Pedro Resende, José Cardoso, Luís Costa, Filipe Falcão, Bernado Bordalo and Joel Puga.

I want to thank Ana Gomes, Mónica Cerquido, Diana Moreira and Andreia Carvalho for all the incredible moments, studying, stressing and laughing. I am really thankful to have their friendship and support, and to share with they some of the best moments of my life.

Finally, I am mostly grateful to my parents and my boyfriend Vítor, for all they have done and do for me! Without they none of this would have been possible, thank for the courage, the comforting words that I often needed as well as their unconditional support. Thank you so much for always being by my side!

Resumo

A construção de micro- e nano-sistemas hipersensíveis que sejam multi-funcionais, de baixa potência e/ou auto-alimentados, para uso em aparelhos eletrónicos pessoais, de monitorização ambiental e da ciência médica, por exemplo, tem vindo a despertar grande interesse.

Para alimentar esses sistemas foram desenvolvidos nanogeradores triboelétricos que convertem energia mecânica em eletricidade através da conjunção do efeito triboelétrico e do efeito eletrostático. Estes nanogeradores caraterizam-se pelo seu potencial na captação da energia das atividades humanas, pneus rotativos, ondas do mar e das marés, vibração mecânica, vento e muito mais. Este tipo de dispositivos tem elevado potencial porque a sua produção é simples, de baixo custo e proporciona elevadas densidades de potência. Os nanogeradores triboelétricos podem ser fabricados pelo empilhamento de duas folhas de materiais feitos de polímeros com diferentes polaridades triboelétricas, com elétrodos metálicos na parte inferior e superior da estrutura montada. Quando submetidos a forças mecânicas externas, o atrito entre os dois filmes gera a mesma quantidade de cargas mas de sinais opostos nos dois lados. Consequentemente, na interface entre os filmes, é criada uma camada de potencial triboelétrico, em que as cargas triboelétricas geradas são separadas por uma pequena distância.

Neste trabalho foi desenvolvido um gerador triboelétrico rotativo que capta energia a partir do fluxo de água, em que inicialmente foi utilizado o PTFE e Nylon 6.6 como par de materiais triboelétricos. O dispositivo constituído por apenas um suporte (com uma placa de Nylon e uma placa de PTFE), atingiu potenciais mais elevados para um fluxo de água de 30 L/min, com uma média de picos de tensão em circuito aberto de $\sim$ 90.3 V, uma corrente de curto-circuito de $\sim$ 79.6 μA e a sua densidade de potência atingiu $\sim$ 4.5 W/m^2. Quando a sua configuração triboeléctrica foi constituída por duas placas de Nylon e uma placa de PTFE, obteve-se um valor médio dos picos de tensão de $\sim$ 69.6 V, uma corrente de curto-circuito de $\sim$ 53.9 μA e uma densidade de potência máxima de $\sim$ 2.3 W/m^2 para 30 L/min. Por último, quando o nosso dispositivo tinha quatro suportes (quatro placas de Nylon e uma placa de PTFE), os potenciais mais elevados também ocorreram para 30 L/min, com um valor médio dos picos de tensão de $\sim$ 75.3 V, uma corrente curto-circuito de $\sim$ 77.7 μA e uma densidade de potência de $\sim$ 4.1 W/m^2. Em seguida, determinou-se qual a melhor estrutura para a captação

de energia efectiva através do movimento da água, e conclui-se que com quatro placas de Nylon, o desempenho do dispositivo é elevado tendo uma potência por segundo de $\sim$ 153.7 mW/s e uma potência por ciclo de $\sim$ 11.0 mW/ciclo para 30 L/min.

Para melhorar o desempenho deste dispositivo, foi substituído o filme de PTFE por um filme de PDMS com a sua superfície texturizada com dois padrões diferentes. O primeiro foi fabricado utilizando um molde de Silício com um padrão de micro-pirâmides. A segunda texturização foi feita utilizando uma amostra de alumínio anodizado com matrizes hexagonais ordenadas na sua superfície. Para estudar e comparar a influência da texturização na superfície do PDMS foi utilizado um sistema de teste sistemático desenvolvido pela Carla Alves no âmbito da sua tese de Mestrado. Deste modo, pode-se verificar que a texturização das superfícies do filme de PDMS conduz a um aumento dos picos de tensão para o dobro.

Os resultados obtidos neste trabalho abrem portas para o desenvolvimento e otimização de geradores triboelétricos num futuro próximo, juntamente com a possibilidade de aplicação destes dispositivos como sensores para monitorizar sistemas de abastecimento de água que possam funcionar, e enviar dados, com recurso à energia que o movimento da água produz nas canalizações.

Palavras-chave

Triboeletricidade; nanogeradores triboelétricos; eletrificação por contacto; indução eletrostática; captação de energia; tribo-cargas; materiais triboelétricos; superfícies micro-estruturadas; padrão nanométrico; fluxo de água.

Abstract

There has been a growing interest in building hypersensitive micro- and nano-systems that are multi-functional, low-power and/or self-powered, for use in personal electronics, environmental monitoring and medical science, for example.

To feed such systems, triboelectric nanogenerators (TENG) were recently developed, converting external mechanical energy into electricity by the conjunction of triboelectric and electrostatic effects. They have the potential to harvest energy from human activities, rotating tires, ocean waves and tides, mechanical vibration, wind, and more. This type of devices has high technological potential because their manufacture is simple, low cost and achieves high power densities. Triboelectric nanogenerators can be manufactured by stacking two sheets of materials made of polymers with different triboelectric polarities, having metallic electrodes on the bottom and top of the assembled structure. When subjected to external forces, friction between the two polymeric films generates the same amount of charges of opposite signs on the two sides. Consequently, a triboelectric potential layer is created at the interface between the films, where the generated triboelectric charges are separated by a small distance.

In this work, we developed a rotary TENG that harvests energy from water flow using PTFE and Nylon 6.6 as the pair of triboelectric materials. The rotary TENG with just one bracket (one Nylon plate and one PTFE plate), reached electrical output values higher for a water flow of 30 L/min, with a mean of open-circuit voltage of $\sim$ 90.3 V, a short-circuit current of $\sim$ 79.6 μA and its power density reached $\sim$ 4.5 W/m^2. When the triboelectric configuration was constituted by two Nylon plates and one PTFE plate, we obtained a mean value of the voltage of $\sim$ 69.6 V, a short-circuit current of $\sim$ 53.9 μA and a maximum power density of $\sim$ 2.3 W/m^2 for 30 L/min. Lastly, when the rotary TENG was constituted by four Nylon plates and one PTFE plate, the higher electrical outputs also occurred for 30 L/min, with a mean value of the voltage $\sim$ 75.3 V, a short-circuit current $\sim$ 77.7 μA and a maximum power density of $\sim$ 4.1 W/m^2. Then, we determined which was the best structure for the effective energy harvesting through water movement and we concluded that with four Nylon plates the performance of the device is higher, with a power per second $\sim$ 153.7 mW/s and power per cycle $\sim$ 11.0 mW/cycle for a water flow of 30 L/min.

To improve the performance of this device, we replaced the PTFE film by a textured PDMS film. The surface modification of the PDMS film was performed by two different ways. The first used a Silicon mold with a pattern of micro-pyramids. The second texturization was performed using an anodic aluminum template with ordered hexagonal arrays of pits at its surface. To study and compare the influence of texturing the PDMS surface with respect to a non-structured PDMS film, we used a system developed by Carla Alves under her Master's thesis for systematic testing. Thereby, we found that, with textured surfaces of the PDMS film by the two methods used, there is a doubling of the mean voltage.

The results obtained in this work open doors for the future development and optimization of these devices, along with the possibility for applying them as sensors to monitor water supply systems that can work and send data using the energy produced by water movement in plumbing.

Key-words

Triboelectricity; triboelectric nanogenerators; contact electrification; electrostatic induction; energy harvesting; tribo-charge; triboelectric materials; micro-structured surfaces; nanoscale pattern; water flow.

Contents

List of Figures

List of Tables

Abbreviations

Al	**Al**uminum
AAO	**A**nodic **A**luminum **O**xide
CEMUP-MNTEC	**Ce**ntro de **M**ateriais da **U**niversidade do **P**orto - Unidade de Micro e Nanofabricação
IFIMUP-IN	Instituto de Física de Materiais da UP - Instituto Nanociência e Nanotecnologia
ITO	**I**ndium **T**in **O**xide
NG	**N**ano**g**enerator
PDMS	**P**oly**d**i**m**ethylsiloxane
PE	**P**oly**e**thylene
PET	**P**oly**e**thylene **t**erephthalate
PMMA	**P**oly(**m**ethyl **m**meth**a**crylate)
PTFE	**P**oly**t**etra**f**luoro**e**thylene
PVC	**P**oly**v**inyl **c**hloride
Si	**S**ilicon
TEG	**T**ribo**e**lectric **G**enerator
TENG	**T**ribo**e**lectric **N**ano**g**enerator
UP	**U**niversidade do **P**orto

Physical Constants

Permittivity of free space	ϵ_0	$=$	8.854×10^{-12} Fm^{-1}

Symbols

P	power	W (Js^{-1})
C	capacitance	F (CV^{-1})
V_{OC}	open-circuit voltage	V
I_{SC}	short-circuit current	A
Q	charge transferred	C
d_0	effective dielectric thickness	m
ϵ_0	permittivity of free space	Fm^{-1}
ϵ_r	relative dielectric constant	Dimensionless
σ	surface charge density	Cm^{-2}

Para os meus pais

e para o Vítor.

Chapter 1

Introduction

Excessive consumption of fossil fuels and the great threat of environmental pollution have been responsible for the great need to develop new technologies that enable the capture of green energy from the environment [1, 2]. On the other hand, the massive development of the world electronic technology in the last years follows a general trend of miniaturization, portability, and functionality. The development of computers is a typical example of miniaturization and handheld cell phones are a typical example of portable electronics. The near future development is about electronics that are increasingly smaller and operate at ultra-low power consumption, making it possible to be powered by energy harvested from our living environment [3]. Therefore, power sources are desperately needed for sustainable, independent, maintenance-free and continuous operation of such small electronics, which could be used widely for implantable biosensors, nanorobotics, remote and mobile environmental sensors, infrastructure environmental monitoring and mobile electronics [3]. Thus, new areas on nanoenergy generation through energy harvesting are emerging for applications of nanomaterials and nanotechnologies in powering micro/nano-systems. The goal is to build self-powered nano-systems with ultra small size, hypersensitivity, multi-functionality, low consumption and self-powered. The general characteristics of such power sources include availability, efficiency and stability [3]. As a solution, nanogenerators (NGs) have been developed to take advantage of everpresent energy such as the movement of the waves or the simple walk of each individual [3, 4]. Recently, triboelectric nanogenerators have been invented as a new approach to harvest energy based on the coupling of triboelectric and electrostatic effects. These nanogenerators are one of the

most promising energy conversion systems because their manufacture is simple, low cost and achieve a high power density [3–8]. Triboelectric nanogenerators can be used to harvest energy using the motion of fluids, such as liquids and gas flows [5]. Thus, these structures can be used to harvest energy from water flows [6] without building a dam. This can avoid the great environmental impact associated with dams (destruction of fauna and flora) and reduces significantly reduce energy cost [9]. Triboelectric nanogenerators can also be used, for example, to harvest the wind energy [5] without the use of wind turbines. This reduces the high cost for its implementation and the environmental impacts of wind farms [10] (such as visual impacts and the significant audible noise of large turbines). A large advantage of triboelectric nanogenerators is that they are small devices, so they have a generally insignificant environmental impact. However, they are not yet suitable for energy harvesting at a large scale.

1.1 Motivation

Triboelectric nanogenerators were recently developed by Dr. Zhong Lin Wang's group and the simplicity in the working mechanism of these nanogenerators, the low cost of manufacture, their ability to achieve a high power density, complementing the great need for green energy harvested from the environment, the ability of harvesting energy from a wide range of sources and under various conditions [3–6], led us of chose them for this Master's thesis. Our goal was to develop a device that uses small water flows that are not used by other large infrastructure (dams, for example) to harvest energy.

Motivated by the previous works of Dr. Wang's group about triboelectric nanogenerators and taking advantage of the IFIMUP-IN and Physics and Astronomy Department resources, the main aim of this thesis was to develop a triboelectric nanogenerator that harvest energy from the motion of water.

1.2 Nanogenerators

Different nanogenerators using different physics effects have emerged in the last years and were used to build a variety of self-powered systems. These nanogenerators are the best

solution to harvest energy from the environment through a clean process. For this, they are arousing great interest worldwide. In particular, thermoelectric, piezoelectric and triboelectric effects allow energy harvesting from the environment for clean electricity production [2, 3].

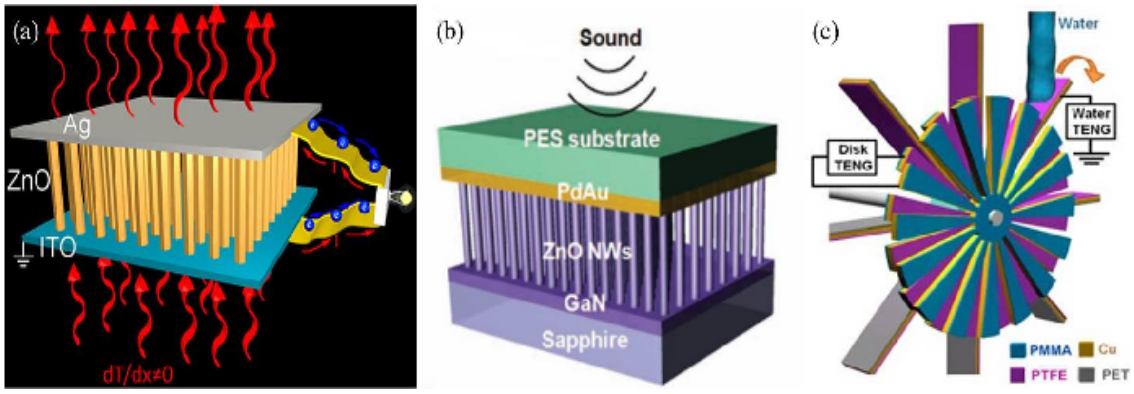

FIGURE 1.1: Working principle of: (a) Thermoelectric nanogenerators (adapted from Yang *et al.* [11]); (b) Piezoelectric nanogenerators (taken from Cha *et al.* [12]); (c) Triboelectric nanogenerators (taken from Cheng *et al.* [13]).

1.2.1 Working Principles

A **thermoelectric nanogenerator** [Fig. 1.1(a)] is an energy harvesting device that uses the thermoelectric effect to convert thermal energy into electrical energy. Normally, the Seebeck effect is used to harvest thermal energy, in which an electric potential is generated between two different metals at different temperatures. The generated voltage measured between the two ends of the junction is proportional to the corresponding temperature difference with a proportionality constant known as Seebeck coefficient. The presence of this temperature gradient is critical for conventional thermoelectric devices because it is difficult to maintain a high-temperature difference between the ends in a miniaturized form [11]. Some of the thermoelectric materials used in this type of device include lead telluride (PbTe), bismuth telluride (Bi_2Te_3) or cadmium telluride (CdTe) [11].

The **piezoelectric effect** allows the creation of an electric potential by means of the deformation of a material, or vice versa. The application of a compressive or tensile force to a non-centrosymmetrical crystalline material leads to a displacement in the negative and positive centers of charge, inducing a piezoelectric polarization and opposite charged surfaces in the

material. The obtained electrical energy can then be injected into external circuit directly from two contacts [14]. A piezoelectric nanogenerator [Fig. 1.1(b)] is then an energy harvesting device converting external kinetic energy into an electrical energy based on energy conversion by nano-structured piezoelectric materials. Some of the piezoelectric materials used in this type of device include barium titanate ($BaTiO_3$), lead titanate ($PbTiO_3$), lead zirconium titanate (PZT) or zinc oxide (ZnO) [14, 15]. However, the output power of this type of nanogenerators is from a few mV to a few V.

Finally, a **triboelectric nanogenerator** [TENG; Fig. 1.1(c)] is an energy harvesting device that converts external mechanical energy into electricity by a conjunction of triboelectric effect and electrostatic induction through periodical contact-separation or relative sliding between two materials with opposite tribo-polarity [3, 7, 8, 13, 16–18]. This new promising technology recently appeared and that produce higher output power. A triboelectric nanogenerators is basically composed by two triboelectric materials with different polarity, an air gap between them and two metal electrodes. When two triboelectric surfaces with opposite triboelectric charges are periodically contacted and separated, a potential difference between the metal electrodes of the two triboelectric surfaces is created, driving electrons to flow between the two metal electrodes [13, 16].

When two different materials come into contact, chemical bonds are formed between them (adhesion). At the same, there is a movement of charges (electrons or ions/molecules) of a material to the other. After the separation of the two materials, some bonded atoms retain extra electrons, while others have a tendency to give them away, producing triboelectric charges on the surface [3]. This triboelectric charges are only confined on the surface of the materials and they neither recombine nor get annihilated. They stay in a quasi-permanent way for an extended period of time although minor charge migrations do occur.

This way, it is possible to formulate a *triboelectric series* (Fig. 1.2) [19] in which the materials are ordered according to their polarity, as in Fig. 1.2. The first triboelectric series was published in 1757 by John Carl Wilcke [3, 20]. In it, the two most distant materials from one another have the highest charge transfer between them. On the other hand, materials near each other have an insignificant charge transfer. Materials with positive charge tendency [such as glass, wool, silica, aluminium or Poly(methyl methacrylate) (PMMA)] lose electrons

when coming into contact with materials of opposite tendency [such as PET (Polyethylene terephthalate), Kapton, PTFE (Polytetrafluoroethylene) or PDMS (Polydimethylsiloxane)] which gain electrons in the process [19].

The TENG is a new concept of innovative energy harvesting with a large number of potential applications because irregular mechanical energy sources, such as human motion, walking, vibration, mechanical triggering, rotating tires, wind, ocean waves and tides, are highly common and available energy sources in our surroundings [3]. For example, the ocean waves and tides have huge amounts of inexhaustible mechanical energy that furthermore does not depend on the weather, climate and daytime like solar energy.

Triboelectrification is one of the most common effects in our daily life and TENG is an updated progress with potential applications as a new energy technology.

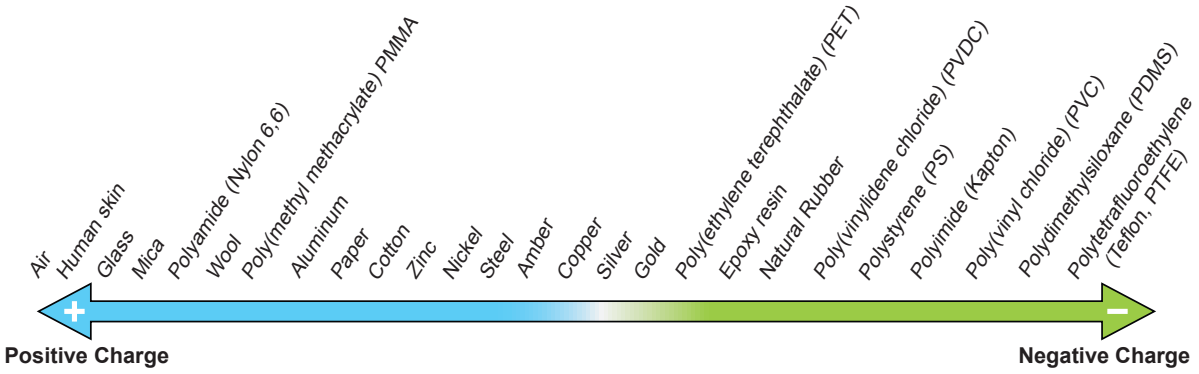

FIGURE 1.2: Triboelectric series (adapted from [3, 19]).

1.3 Thesis Organization

In this first chapter, we introduced the concept of nanogenerators, their most usual types and working principles. Then, we briefly introduced the triboelectric nanogenerator and possible pairs of triboelectric materials. In Chapter 2 we will introduce the theory of triboelectrification and describe in detail the triboelectric nanogenerator. Subsequently, we will describe the four different basic modes and mechanisms of TENGs. Lastly, we will detail the importance of the selection of materials and the influence of different surface morphologies on the

energy generated by the TENG. Chapter 3 explores the evolution of producing our TENG, where we will mention our motivation for the development of our device and the modifications for its optimization. Furthermore, we will describe the production methods used for fabrication of the triboelectric materials used in this device. Afterwards, in Chapter 4 we will describe the systematic testing method that we developed to reliable and reproducibly data to evaluate the performance of our TENG. We will also explore and describe the devices developed and used to measure the electrical outputs. Finally, Chapter 5 describes the working mechanism of our rotary TENG and presents the results obtained in this work and their subsequent discussion. We will also refer the best triboelectric configuration for the rotary TENG operation. Finally, in Chapter 6, we will present the concluding remarks on the herein described project and future work.

Chapter 2

Triboelectric Nanogenerators

2.1 Introduction to Triboelectrification

Triboelectrification is an effect that is known since ancient Greek time. The prefix *tribo* is derived from the Greek word ”tribos” that mean *rubbing*, referring to ”friction”, as in tribology [19, 21]. On the other hand, Tales de Mileto originally suggested the word ”electricity” (from William Gilbert’s initial coinage, ”electra”) from the Greek word for amber, *elektron*.

Tribology is defined as the science and technology of interacting surfaces in relative motion and comprises the study of friction, wear and lubrication [21]. Whenever two objects touch each other, forces of action and reaction are brought into play and a surface interaction occurs [22]. When two objects are in contact it is necessary to apply a force in order to separate them. If the area of true contact is small, the force is negligible, which would not be the case if the contact area was extensive. For this reason, the forces of adhesion commonly measured are often attributed to van der Waals forces. However, it was demonstrated that electrostatic forces and charge transfer were responsible for most adhesion, but it is not clear if the electrostatic forces are important when previously charged objects are brought together [23].

The triboelectric effect is thus one of the few effects that have been known for thousands of years and is also one of the most frequently experienced effects that each and every one of us inevitably encounters every day. Triboelectricity can cause discharges that damage

several industrial processes, electronics and even cause wild fire in nature [24]. This effect happens when two surfaces of certain materials (with different triboelectric polarities) are brought into contact and separated and the transfer of charge from one surface to the other occurs).

Three different surface charging mechanisms have been investigated in recent years: electron transfer, ion partition between surfaces and mass transfer [25]. For example, when two metals contact each other, electron transfer from one surface to the other occurs. Physically, the electrons tunnel from the metal of lower work function to the metal of higher work function until the Fermi levels of the two are equal (Fig. 2.1) [19, 26, 27]. In Fig. 2.1, ϕ_1 is the work function of metal 1, ϕ_2 is the work function of metal 2 and e is the elementary charge.

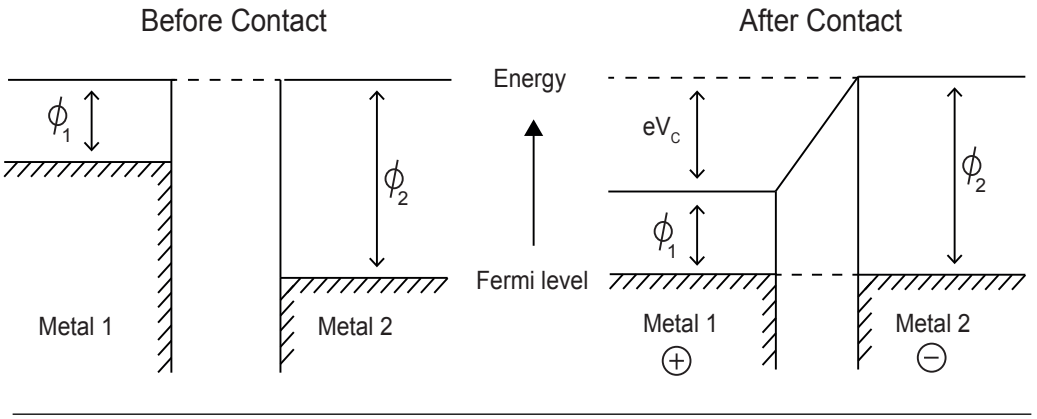

FIGURE 2.1: Charge transfer between two metals for metal-metal contact [27].

On the other hand, when there is contact between a metal and an insulator, studies indicate that the insulator's surface has a charge saturation point. This point occurs when the electrons tunnel from the metal to the surface of insulator and there is a raise of the characteristic energy level of the insulator above the Fermi level of the metal [19]. For the tribocharging of insulators, this is not caused by the tunneling of electrons. However, studies have shown that chemical reduction reactions occur on the surface of polymers such as PTFE, PMMA and PE [19]. These reactions are responsible for the transference of material and adsorption of ions to polar groups on the surface of insulating, but it is still uncertain whether electron transfer also occurs [19, 26].

The first triboelectric nanogenerator was invented in January 2012 by Fan *et al.* and had the form of a sandwich structure as shown in Fig. 2.2(a). It gave an output voltage of up

to 3.3 V at a power density of $\sim$10.4 mW/cm^3 [3, 24, 28]. This device was composed by two sheets of different polymeric insulating material stacked alternatively without interlayer binding. The two flexible thin films were made of Kapton and PET and the contact area between them were non-uniform, with different roughnesses of the order of hundreds of nanometers [28].

As shown in Fig. 2.2(b), since TENGs were reported, their output power density increased 5 orders of magnitude in the first 12 months [3]. This increased is due to the optimization of the surface morphologies of materials at the micro/nano-scales, including the use of nanowires, nanoparticles or nanopores [3, 4, 13, 29].

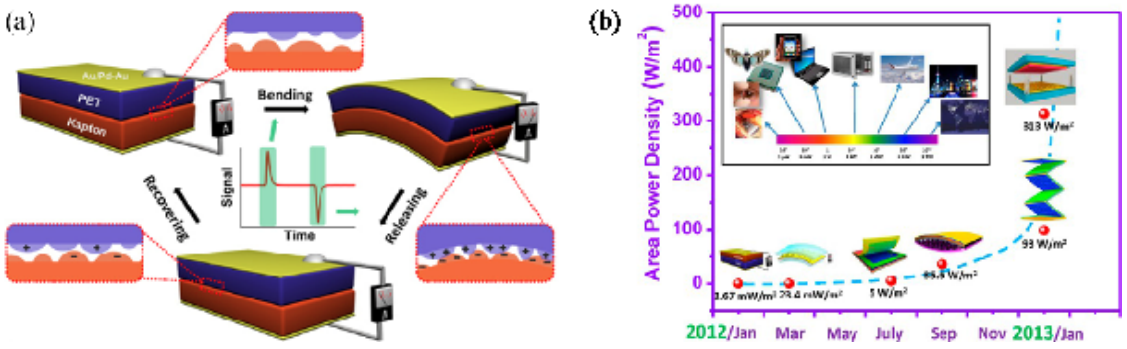

FIGURE 2.2: Triboelectric nanogenerators: (a) Schematic illustration of the structure and working principle of the first triboelectric generator (taken from Fan *et al.* [28]); (b) Summary on the progress made in the output power density of triboelectric nanogenerators within 12 months [3].

2.2 Theory of triboelectric nanogenerators

2.2.1 Inherent capacitive behavior and V–Q–x relationship

The working principle of an arbitrary TENG is a conjugation of contact electrification and electrostatic induction and these devices will have fundamentally an inherent capacitive behavior. When TENG are subjected to periodic external forces/movements, a potential difference is created on the electrodes due to charge transfer between the two triboelectric materials. Thus, free electrons are conducted in the two electrodes to flow between them in order to balance the induced potential difference. If the transferred charges from one electrode to another is defined by Q, the transferred charge of each electrode is -Q and +Q. The transferred

charge Q of each electrode and the polarized triboelectric charges at the contact contribute to electrical potential difference between the two electrodes. The separation of the tribo-charges contributes to the voltage $V_{OC}(x)$, which is a function of the separation distance *x* between the two triboelectric layers. Assuming a typical capacitor (when no triboelectric charges exist), the contribution of the transferred charges between the two electrodes to the electrical potential difference is -$\frac{Q}{C(x)}$, where C is the inherent capacitance between the two electrodes. Through the electric potential superposition principle, the total voltage difference between the two electrodes is given by the V-Q-x relationship [30]:

$$V = -\frac{1}{C(x)}Q + V_{OC}(x). \tag{2.1}$$

Under short-circuit conditions, these transferred charges (Q_{SC}) represent the electrical potential generated from the polarized triboelectric charges. Hence, Eq. (2.1) under short-circuit conditions becomes [30, 31]:

$$Q_{SC} = C(x)V_{OC}(x). \tag{2.2}$$

2.3 Basic Modes and Mechanisms

TENGs are classified by the different configurations of the electrodes and/or different motion of the triboelectric materials to realize their fundamental electrostatic induction process. Four different modes have so far been realized [3, 30, 32–35].

2.3.1 Vertical Contact-Separation Mode

The vertical contact-separation mode-based TENG is mainly divided into two categories: dielectric-to-dielectric and conductor-to-dielectric types [Fig. 2.3(a) and (b), respectively] [30, 31].

Figure 2.3(a) illustrates an example of the working mechanism for a TENG in the dielectric-to-dielectric vertical contact-separation mode, when using two similar dielectric films and two electrodes deposited on the top and the bottom surfaces of the stacked structure.

Where dielectric 1 and 2 are defined as having a thickness of d_1 and d_2, respectively. In the initial state [Fig. 2.3(a)-I], the two materials have no triboelectric charges on their surfaces. In this case, when an external force is applied on the device (bending or pressing the device) [Fig. 2.3(a)-II], the distance (x) between the two triboelectric materials with different triboelectric polarities will vary and they come into contact with each other [3, 30, 36]. At that time, charge

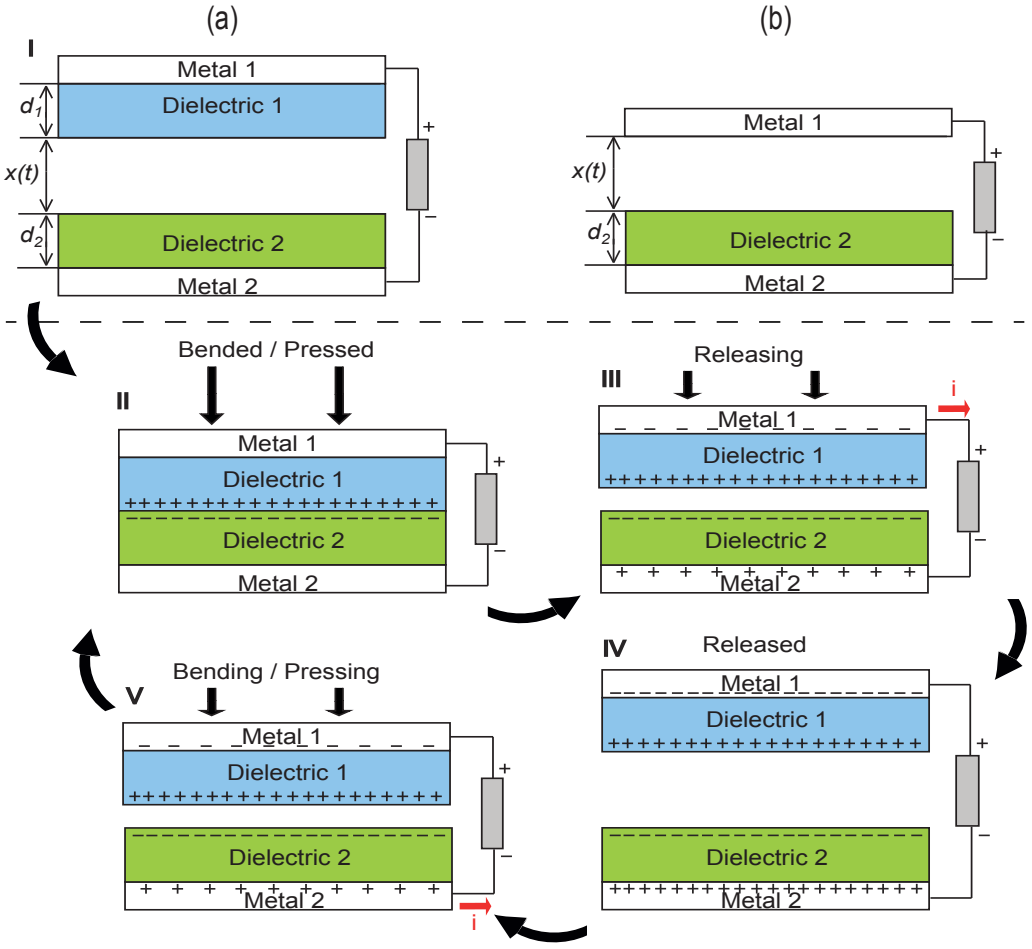

FIGURE 2.3: Vertical Contact-Separation Mode-Based TENG (adapted from [3, 30, 31]): (a) dielectric-to-dielectric; (b) conductor-to-dielectric.

transfer begins in the contact area due to triboelectrification [3]. This way, one side of the surface will have positive static charges and the other negative static charges, with equal density of σ. For insulators is reasonable to assume that the tribo-charges are uniformly distributed in the two surfaces. Removing the applied force [Fig. 2.3(a)-III], the distance x starts to increase

and the two surfaces with opposite charges are separated. Therefore, a potential difference is induced between the upper and lower electrodes and the instantaneous amount of charges on each electrode is +Q and -Q [30]. The electrons are then conducted to flow from one electrode to the other (positive current) trough the external load [3]. Thus, the induced charges accumulate with negative sign on the top electrode and positive sign on the bottom electrode [Fig. 2.3(a)-IV]. When an external force is applied again, decreasing the distance between the two triboelectric materials and consequently, electrons are driven from the top electrode back to the bottom electrode (negative current) and the amount of induced charges are reduced [Fig. 2.3(a)-V]. When the two triboelectric materials return to the initial state, all induced charges are neutralized [Fig. 2.3(a)-II] [3, 24].

In Fig. 2.3(b) the working mechanism is very similar but Dielectric 1 is replaced by metal 1 that plays two major roles: triboelectric layer and electrode [30]. Consequently, the total charges in the metal 1 results from the contribution of the triboelectric charges ($S\times\sigma$; S is area size of metal) and the transferred charges between the two electrodes (-Q). Therefore, in metal 1 there is Sσ-Q of the total charges. Assuming that the electrodes are infinitely large because S, in the experimental case, is several orders of magnitude larger than d_1+d_2+x, one has [30, 31]:

$$V = -\frac{Q}{S\epsilon_0}(d_0 + x(t)) + \frac{\sigma x(t)}{\epsilon_0}, \tag{2.3}$$

giving the open-circuit voltage:

$$V_{OC} = \frac{\sigma x(t)}{\epsilon_0}, \tag{2.4}$$

the short-circuit charge:

$$Q_{SC} = \frac{S\sigma x(t)}{d_0 + x(t)}, \tag{2.5}$$

where, ϵ_0 is the permittivity of free space and d_0 is the effective dielectric thickness given by [30]:

$$d_0 = \frac{d_1}{\epsilon_{r1}} + \frac{d_2}{\epsilon_{r2}}, \tag{2.6}$$

where, ϵ_{r1} and ϵ_{r2} are the relative dielectric constants of dielectric 1 and 2.

Triboelectric nanogenerators based on the vertical contact-separation mode works by an intermittent impact or shock and is used to harvest energy from engine vibration or human walking, for example. This mode is characterized by a simple structural design and high instantaneous power density [24].

2.3.2 Lateral Sliding-Mode

The sliding-mode TENG has the same structure as the vertical contact-separation mode and also has two types: dielectric-to-dielectric and conductor-to-dielectric [Fig. 2.4(a) and (b), respectively] [30]. In Fig. 2.4(a) and (b), the bottom part is fixed, while the top could slide along the longitudinal direction. In this mode there are two basic friction processes: normal contact and lateral sliding [Figure 2.4(a)] [3]. Assuming that the thickness of whole structure is much smaller than the its transversal width *w*, it is possible to use a 2D model to simplify the calculations. Let us consider that d_1 and d_2 are the thicknesses of the two dielectrics, *l* is the length in the longitudinal direction and *x* is the lateral separation distance. When two materials with different tribo-polarity are in contact, a relative sliding parallel to the surface also creates triboelectric charges on the two surfaces [Fig. 2.4(a)-I]. Such as in the previous mode, it is reasonable to assume that the tribo-charges are uniformly distributed on the insulators surface (with tribo-charges decay neglected). At the surface of dielectric 1 the surface charge density is σ and at the surface of dielectric 2 is -σ. The total charge at each metal electrode under open-circuit (OC) conditions is 0 and if Q is the transferred charge, the total charge amount on metal 1 and metal 2 is -Q and Q, respectively [30]. A lateral polarization is then introduced along the sliding direction by a periodic change in the contact area (when is an external mechanical force applied), which creates a potential difference across the two electrodes. Consequently, a current flow from the top electrode to the bottom electrode will appear in order to generate an electric potential drop that cancels the tribo-charge-induced potential [Fig. 2.4(a)-II] [3]. This flow of current continues until the two triboelectric materials are completely separated [Fig. 2.4(a)-III]. Afterwards, the dielectric 1 moves inwards relative to dielectric 2, which results in current in the external circuit with the opposite sign of that of the sliding out process [Fig. 2.4(a)-IV]. When the two dielectrics return to the overlapping position, the charged surfaces get in fully contact, thereby again initiating the cycle [Fig. 2.4(a)-I] [3].

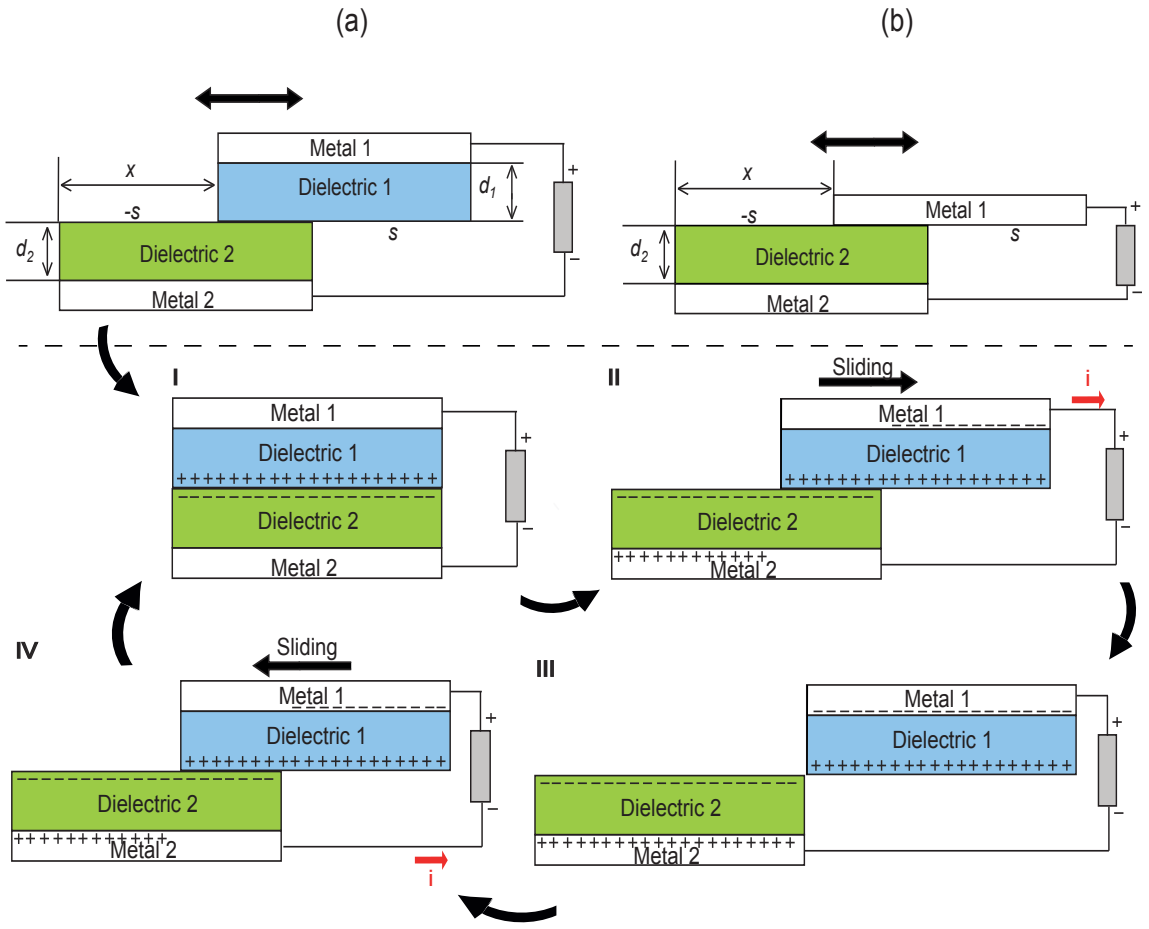

FIGURE 2.4: Lateral Sliding-Mode-Based TENG (adapted from [3, 30]): (a) dielectric-to-dielectric; (b) conductor-to-dielectric.

Since the length of the dielectrics is much larger than their thickness and the two dielectrics are not thoroughly separated, the dominant part of the total capacitance is the capacitor between the overlapped region. The total capacitance can be estimated by the parallel-plate capacitor model as [30, 31]:

$$C = \frac{\epsilon_0 w(l-x)}{d_0}, \tag{2.7}$$

where d_0 is the effective dielectric thickness as previous defined.

Considering that the electrodes work as infinite plates in each region when the length

of the dielectric layers is much larger than their thickness, the charge distribution is uniform in each region and along the y-direction inside the dielectrics layers, and thus the electric field is uniform. In an ideal case, for the non-overlapped region, σ is the absolute value of the surface charge density. For the overlapped region, the charge density is still uniform. The ideal charge distribution ρ under OC condition is [30]:

- for the non-overlapped region of the bottom dielectric: ρ = σ;
- for the overlapped region of the bottom dielectric: ρ = -$\frac{\sigma x}{l-x}$;
- for the non-overlapped region of the top electrode: ρ = -σ;
- for the overlapped region of the top dielectric: ρ = $\frac{\sigma x}{l-x}$;

Using Gauss' Theorem and the previous charge distribution, V_{OC} is given by [30, 31]:

$$V_{OC} = \frac{\sigma x d_0}{\epsilon_0 (l - x)}. \tag{2.8}$$

Therefore, the V-Q-x relationship for lateral sliding-mode TENGs is given by [30]:

$$V = -\frac{1}{C}Q + V_{OC} = -\frac{d_0}{w\epsilon_0 (l - x)}Q + \frac{\sigma d_0 x}{\epsilon_0 (l - x)}s. \tag{2.9}$$

For the conductor-to-dielectric type, the structure is as shown in Fig. 2.4(b) and, in this case, metal 1 is the triboelectric layer and also one of the electrodes itself [30].

For the sliding mode, the energy conversion efficiency and device durability are essential issues, and can be limited by the relatively large frictional resistive force between triboelectric surfaces during operation the of the triboelectric nanogenerator [37]. However, this mode has several advantages compared to the vertical contact-separation mode. The relative sliding between two triboelectric surface is more effective for the generation of tribo-charges than the pure contact, and consequently there is an enhanced output power [24].

The mechanism of in-plane charge separation can work in either directional sliding between two plates, cylindrical rotation or disc rotation mode [3, 24].

2.3.3 Single-Electrode-Mode

A single-electrode based triboelectric nanogenerator was introduced as a more practical and feasible design for some applications because, for the previous modes discussed, both of the triboelectric layers need to be connected to an external circuit, which limits TENGs' versatility and applicability [24]. This energy harvesting strategy can occurs both in the contact-separation mode and contact-sliding mode [3, 38] [Fig. 2.5(a) and (b), respectively]. The working principle of a single-electrode TENG (SETENG) is schematically shown in Fig. 2.5, where we can see that only one electrode (primary electrode) is attached to the triboelectric layer and the other electrode is an electric potential reference (placed anywhere in space) and the ground (called reference electrode) [30].

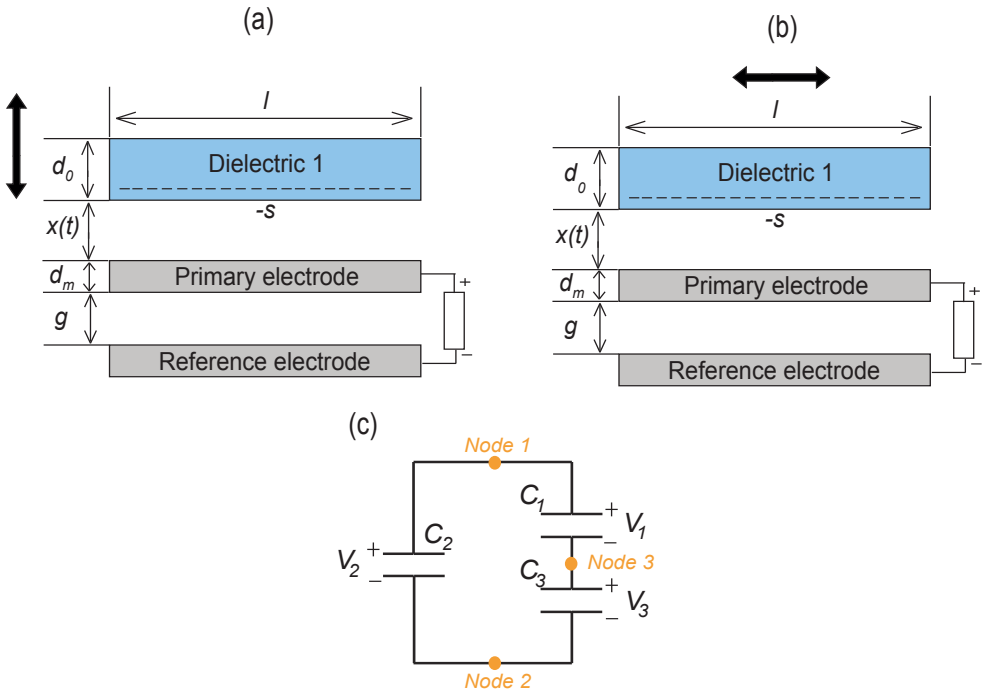

FIGURE 2.5: Single-Electrode-Based TENG (adapted from [30]): (a) conductor-to-dielectric contact-mode; (b) conductor-to-dielectric sliding-mode; (c) Equivalent circuit model with three capacitances under open-circuit condition.

Initially, we will discuss the conductor-to-dielectric contact-mode SETENGs. The primary electrode (metal electrode) is the other triboelectric material and has a width *w* and length *l* (like

dielectric 1) [Fig. 2.5(a)]. Dielectric 1 and the primary electrode have thicknesses d_0 and d_m, respectively. As Fig. 2.5(a) shows, the reference electrode is located underneath the primary electrode (with a gap of *g*) and both have the same geometric size.

In this configuration, when an external force is applied, dielectric 1 moves along the vertical direction, and the distance *x* between dielectric 1 and the primary electrode varies but the two electrodes (primary and reference) are fixed. When the two triboelectric materials come into contact, the triboelectric effect makes the surface of dielectric 1 carry negative tribo-charges (with a density of -σ) and the primary electrode becomes charged by an equal amount of positive charges (σwl) [30]. Such as in the previous modes, it is reasonable to assume for insulators that the tribo-charges are uniformly distributed on its triboelectric surface. The transferred charges from the primary electrode to the reference electrode is Q and, under the minimum achievable charge reference state, the total amount of charges at the primary electrode is σ*wl*-Q and at the reference electrode is Q [30].

Through the analysis of nodes in the electrostatic system shown in Fig. 2.5(c), one can calculate the values of C, V_{OC} and Q_{SC} for the contact-mode SETENG. In OC condition, the electrical potential across the whole bottom surface of dielectric 1 is nearly constant, so that it can be assumed as a node (Node 1). Also, the primary and the reference electrodes serve as two nodes (Node 2 and Node 3, respectively). Between each nodes is formed an equivalent capacitance since each two nodes are connected by electric field lines [Fig. 2.5(c)]. In the equivalent circuit, the capacitances C_1, C_2 and C_3 only represent the capacitive effects from the direct electric line connection between every two nodes without electrostatic shield of the third object [30].

The actual capacitance C_b between Node 1 and Node 3 is given by [30]:

$$C_b = C_2 + \frac{C_1 C_3}{C_1 + C_3}, \tag{2.10}$$

that between Node 1 and Node 2 (C_a) by [30]:

$$C_a = C_1 + \frac{C_2 C_3}{C_2 + C_3}, \tag{2.11}$$

and that between Node 2 and Node 3 (C_0) by [30]:

$$C_0 = C_3 + \frac{C_1 C_2}{C_1 + C_2}. \tag{2.12}$$

The total charges on Nodes 1, 2 and 3, under OC condition, are -σwl, σwl and 0, respectively, and from basic characteristics of capacitances and charge conservation on each node, Q_{SC} and V_{OC} can be calculated [30]:

$$Q_{SC} = \frac{\sigma w l}{1 + C_1(x)/C_2(x)} \tag{2.13}$$

and

$$V_{OC} = \frac{\sigma w l C_2}{C_1 C_2 + C_2 C_3 + C_3 C_1}. \tag{2.14}$$

In the previous equations, the capacitance C_2 is important and represents the portion of the electric lines directly connecting Node 1 and Node 3 (without being electrostatically shielded by Node 2). If all the electric lines connections between the reference electrode and dielectric 1 needs to come through the primary electrode (electrostatic shielded by the primary electrode), C_2 will be equal to 0, which will lead to no output from the SETENG [30]. The electrostatic shield effect of the primary electrode limits the output performance of SETENGs and the maximum charge transfer efficiency can only reach 50 %. However, one of the triboelectric layers can move freely without any restriction [24, 30].

2.3.4 Freestanding Triboelectric-Layer-Mode

A new triboelectric mode called freestanding-triboelectric-layer based triboelectric generators (FTENGs) was recently created [24, 30, 33, 39, 40]. The configuration of this new mode permits to increase the TENGs' versatility and applicability for harvesting energy from any moving object because the object does not need to be connected to the entire system by an interconnect (as the SETENGs). A FTENG is constituted by the tribo-charged surface alternatively approaching two fixed-electrodes.

The freestanding triboelectric-layer mode has two typical configurations: contact-mode (CFTENGs) and sliding-mode (SFTENGs) [30]. In these FTENGs' configuration, the triboelectric layer does not need to maintain the contact with the electrodes during the contact [39] or the sliding and this advantage largely improves the energy conversion efficiency, minimizes the surface wear and the long-term stability of the generator [24].

2.3.4.1 Contact-mode FTENGs

There are two typical subcategories for contact-mode FTENGs with their working principal being very similar: dielectric freestanding layer CFTENG and metal freestanding layer CFTENG [Figs. 2.6(a) and (c), respectively] [30]. The first configuration [Fig. 2.6(a)] has a dielectric layer with thickness d_1 (relative dielectric constant of ϵ_{r1}), two metal layers forming two triboelectric pairs (also serving as electrodes), and between these metallic layers there is air (with a total air gap thickness is *g*).

When an external mechanical force is applied to the dielectric layer, it is forced to contact with the two metal layers and the top and bottom surface of dielectric acquire tribocharges due to the triboelectrification. The triboelectric charge density of both surfaces of the dielectric layer is -σ and, due charge conservation, the two metal layers have the same amount of positive charges in total. Let us assume that the size of the metal electrode is much larger than the air gap, thus the area size (S) of the CFTENG is infinitely large and edge effect can be ignored. Consequently, the electric potential on metal 1, metal 2, the top and bottom surface of dielectric 1 are all constant and the electrostatic system with these 4 surfaces can be seen as having 4 nodes, as shown in Fig. 2.6 (b). However, one only has three capacitances because we assume that S is infinitely large and thus the electrical line connection between two non-adjacent nodes is blocked by the intermediate node. The total capacitances between the two electrodes is given by [30, 40]:

$$C = \frac{1}{(1/C_1) + (1/C_2) + (1/C_3)} = \frac{\epsilon_0 S}{d_0 + g}, \tag{2.15}$$

where d_0 is the effective dielectric thickness as seen previously.

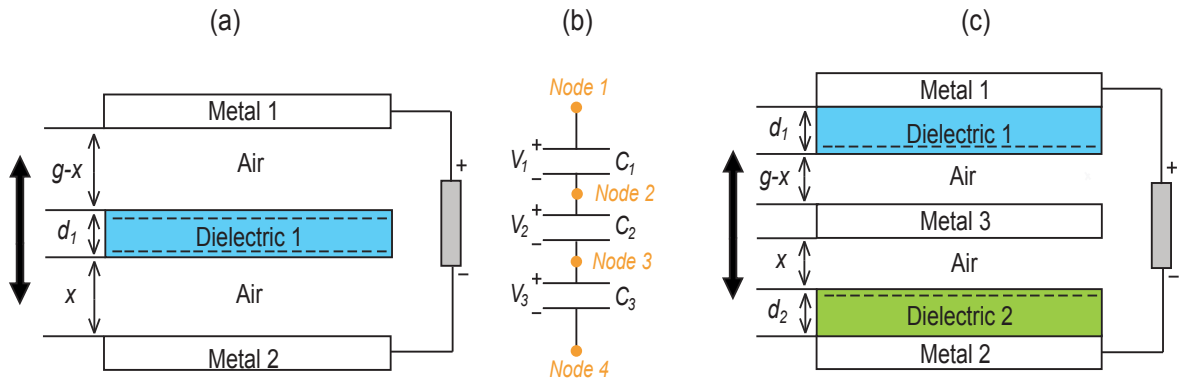

FIGURE 2.6: Contact-mode freestanding TENGs (adapted from [30, 40]): (a) dielectric freestanding layer CFTENG; (b) metal freestanding layer CFTENG.

In short-circuit conditions, Nodes 2 and 3 have a amount of charges (-σS), while the total charges in Node 1 and Node 4 are 2σS due the charge conservation.

The total charge in metal 1 (Q_1) and 2 (Q_2) is determined from the charge conservation and basic electrodynamics theory. Taking into account that, in practical applications, d_1/ϵ_{r1} is negligible compared to the air gap, one has that C_2 is infinitely large. Consequently, we have [30, 40]:

$$Q_1 \approx \sigma S \frac{(2/C_3)}{(1/C_1)+(1/C_3)} = \frac{2\sigma S}{1+(C_3/C_1)} \tag{2.16}$$

and

$$Q_2 \approx \frac{2\sigma S}{1+(C_1/C_3)}. \tag{2.17}$$

The change of the dielectric 1 position induces a variation of the capacitance ratio between the tribo-charged surfaces and the two electrodes that, under short-circuit condition, can drive electrons to flow between the two electrodes. The value of the transferred charges (Q_{SC}) and the open-circuit voltage is given by [30, 40]:

$$Q_{SC} = \frac{2\sigma S x}{d_0 + g} \tag{2.18}$$

and

$$V_{OC} = \frac{2\sigma x}{\epsilon_0}. \tag{2.19}$$

Therefore, the V-Q-x relationship for the CFTENG is [30, 40]:

$$V = -\frac{d_0 + g}{\epsilon_0 S} + \frac{2\sigma x}{\epsilon_0}. \tag{2.20}$$

Figure 2.6(c) shows the metal freestanding layer CFTENG and respective working principle which is very similar to the dielectric case analyzed previously.

2.3.4.2 Sliding-mode FTENGs

There are also two typical subcategories for the sliding-mode FTENGs: dielectric freestanding layer SFTENG and metal freestanding layer SFTENG [30, 40], illustrated in Fig. 2.7(a) and (b), respectively.

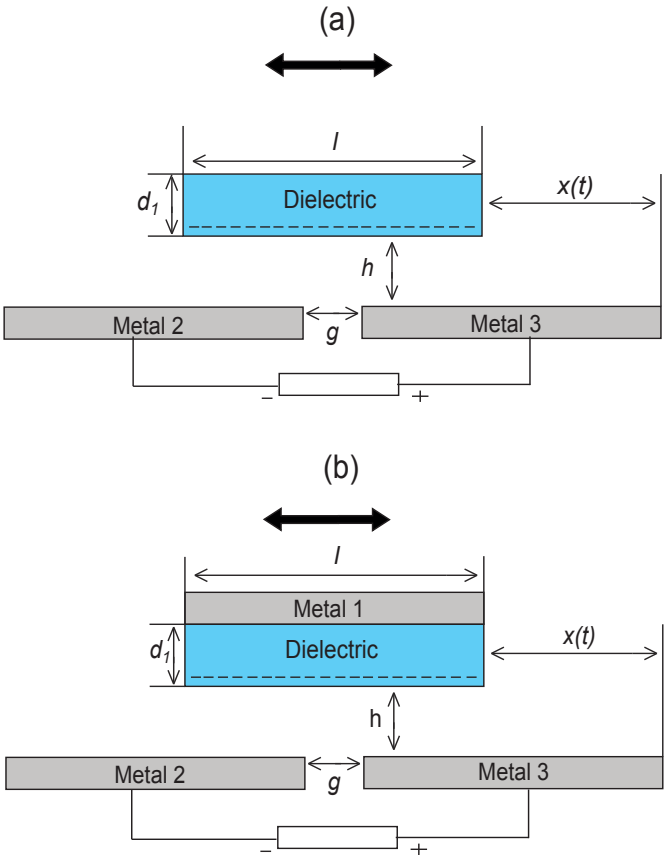

FIGURE 2.7: Sliding-mode freestanding TENGs (adapted from [3, 30]): (a) dielectric freestanding layer SFTENG; (b) metal freestanding layer SFTENG.

These two structures look very similar with the freestanding material strongly influencing the output characteristics of the SFTENGs. Furthermore, the main working principle of SFTENGs is very similar to that of CFTENGS.

Relatively to the structure of SFTENG, the metal 1 and metal 2 are placed as illustrated in Fig. 2.7 to form two electrodes and a freestanding layer (with the same size as the each metallic ones) stands on the top of the electrodes with a distance defined as the freestanding height h [30]. The width of this structure is defined as *w*.

For dielectric SFTENGs [Fig. 2.7(a)], the freestanding material only contains a dielectric, but in the case of metal SFTENGs [Fig. 2.7(b)], the dielectric freestanding material has a thin layer of metal deposited at its top.

The freestanding mode, compared to the lateral sliding-mode, can work without direct physical contact between the two triboelectric surfaces, and it will cause no material wear and heat generation under long continuous working. This mode is characterized by its ultra robustness and high energy conversion efficiency [24].

Seeing the previous equation of the different triboelectric modes, the tribo-charge surface density (σ) is directly proportional to the voltage, transferred charge and current. That is, σ is affected by roughness of the contact surfaces, intrinsic material properties of the two triboelectric layers, and can be increased by a proper choice of triboelectric materials and optimizing the morphology of their surfaces. Consequently the performance of the device can be enhanced.

2.4 Choice of Materials and Surface Structures

In the construction of triboelectric nanogenerators one must consider three main factors to achieve a high performance: device structure, material selection and contact surface morphology. Device structure was already discussed in the last section and we will now detail the other two factors.

The selection of materials to use is based on the triboelectric series because it is important to ensure that the two materials that come into contact with each other have different

triboelectric polarities [41]. In general, most of materials have triboelectrification effects, including metals, polymers and wood. These materials are potential candidates for the fabrication of TENGs, but the ability of a material to gain/lose electrons depends on their polarities [42]: materials with positive charge tendency lose electrons when coming into contact with materials of opposite tendency which gain electrons in the process.

In a triboelectric series, the materials are ordered according to their polarity. Accordingly, the two most distant materials from one another in the series have the highest charge transfer between them [42]. On the other hand, materials near each other have an insignificant charge transfer.

The other parameter that can be used to increase the performance of TENGs is surface morphology. In Fig. 2.8 one can observe some examples of nanopatterns that have been made to increase the effective friction area, and thus the triboelectric effect. The morphologies of the surfaces of the materials can be altered by physical processes by creating pyramid-, square-, micro- or hemisphere-based nanopatterns to increase the contact area between the surfaces of the materials [Figs. 2.8 (a) and (b)] [3, 42–45]. This is because the insertion of

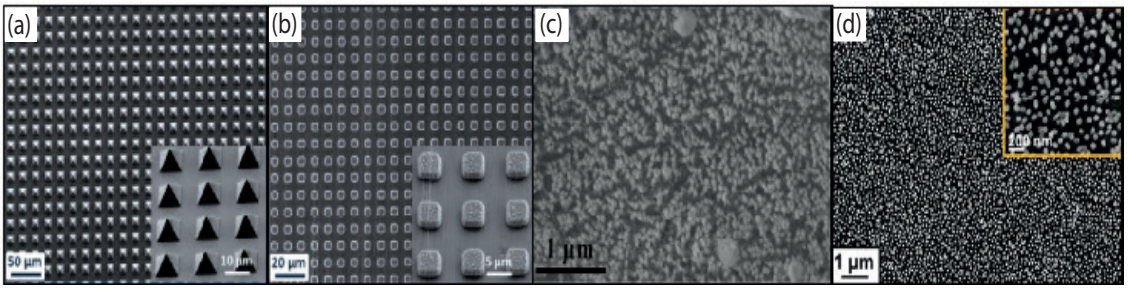

FIGURE 2.8: SEM images of morphologies of the surfaces of the materials: (a) Pyramid nanopatterns (taken from Wang *et al.* [2]); (b) Square nanopatterns (taken from Wang *et al.* [2]); (c) Nanowires patterns (taken from Cheng *et al.* [13]); (c) Nanoparticles patterns (taken from Lin *et al.* [43]).

nanostructures in the surfaces changes the characteristics of the contact areas. However, relatively bulky (micrometer scale) structures on the surfaces can lead to excessive and undesirable friction forces and consequently degrade the energy conversion efficiency of the triboelectric nanogenerator [3]. On the other hand, nanoscale surface morphologies can have critical limitations, such as limited controllability, restricted materials selection, fixed morphologies and weak mechanical properties [46]. So, it is important to note that there can be a reduction of the TENG

energy conversion efficiency when the structure created on the surface is irregular because it can increase the friction force [3].

Another way to increase the triboelectric effect consists in the chemical functionalization of the surfaces of materials [Figs. 2.8(c) and (d), respectively]. A simple surface functionalization can change the triboelectric sequence of the materials in a triboelectric series, which can improves the output performance of triboelectric devices [41]. Thus, the materials used to manufacture TENGs can be composites that can change the electrification of the surface and the permittivity of the material in order to be effective for electrostatic induction [3].

Since the effect of the topography and morphology of nanoscale surface significantly influence the contact characteristics and performances of the devices, there are several approaches to bring about these changes [e.g., anodic aluminum oxide (AAO), surface-linked nanoparticles (NPs) or polymer dry-etching] [46].

In relation to microstructures on the surface of polymers that enhance the electrical output performance of triboelectric nanogenerators, Fan *et al.* [47] made a detailed comparative characterization of the devices with different PDMS features. This group analyzed the open-circuit voltage and short-circuit current output of four different PDMS features: film (unstructured plane), line, cube and pyramid.

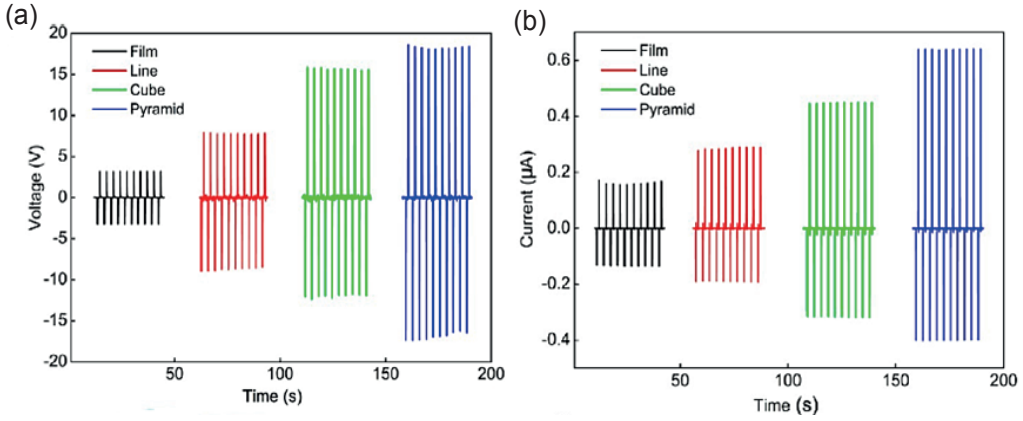

FIGURE 2.9: (a) Output voltage of a TENG using PDMS thin film with unstructured surface and various micropatterned features (taken from [47]). (b) Output current of a TENG using PDMS thin film with unstructured surface and various micropatterned features (taken from [47]).

Figure 2.9 shows the results obtained, where a substantial increase in the electrical output of the structured films over the unstructured films is clear. Particularly, the electrical output of the pyramid-featured device far surpassed (it increases between 5 and 6 times) that exhibited by the unstructured films with similar thickness [47]. To increase the friction area and the efficiency in the power generation process of the device it is important that the pyramid features have a perfect geometric structure and a sharp tip.

This improve of the efficiency of the nanogenerator with structured films can be attributed to the following factors [47]:

- The sophisticated structures on the surface of the films increase the effective triboelectric effect and can generate more surface charges during the friction.

- The presence of air voids and the increase in effective dielectric constant improve the capacitance change in the deformation process. Conversely, when a device is completely sealed with few air voids and weak sliding, there is a rather low output due to the weak friction.

- Additionally, a larger dipole moment is formed in the microstructured films between the electrodes due to the fact that the triboelectric charges are more separated.

Chapter 3

Device Development

In this chapter we explore the evolution of producing our triboelectric nanogenerator. Through the following sections we will mention our motivation for the development of our device and the modifications for its optimization. Furthermore, we will describe the production methods used for the fabrication of some triboelectric materials used in this device, and for the texturing of the surface of a PDMS film.

3.1 Scavenging energy from the motion of fluids

Triboelectric nanogenerators can be used to harvest energy from the movement of fluids, such as liquids and gases using the methods mentioned above. TENGs were shown to harvest energy from drops of rain, the water flowing in a river, tides and waves of oceans [48, 49]. These movements are a huge reserve of renewable mechanical energy, allowing us to mitigate the heavy dependence on limited fossil fuels.

The use of hydroelectric dams allows us to obtain hydro energy as a source of renewable energy [9]. The hydroelectric dams have converters for the movement of water, which rely on normal electromagnetic generators that are bulky, heavy but must be used to achieve a decent output power and conversion efficiency. Furthermore, they also have other essential components such as turbines that further increase system size, complexity and cost. In addition, various natural water movement, especially waves are not suitable for driving a turbine.

The use of TENGs allows a very desirable direct interaction with the various existing water bodies, for the hydraulic energy harvesting though the output powers are not comparable with those obtained by a dam.

Another type of green and renewable energy is wind energy, which arouses great interest in building triboelectric nanogenerators to harvest this type of energy. The wind kinetic energy is an energy source that can be transformed into electricity through the use of wind fans. However, this conventional approach to power generation depends on the turbines structure, showing some disadvantages of this type of device (including the weight and large size, manufacturing complexity, high installation cost and limitation in the case of weak wind [10]). The fact that this device has limitations to produce electricity from wind with low amplitude, means that there is a great need to extend this type of energy harvesting in our living environment. Through the development of TENGs it is possible to harvest weak wind energy. The triboelectric NGs are particularly suitable to power small electronic devices and/or sensors. Just as an example, the prevalence of natural gas in modern metropolitan life and the need for ventilation control systems makes wireless gas meter reading required [50]. Through the use of triboelectric NGs

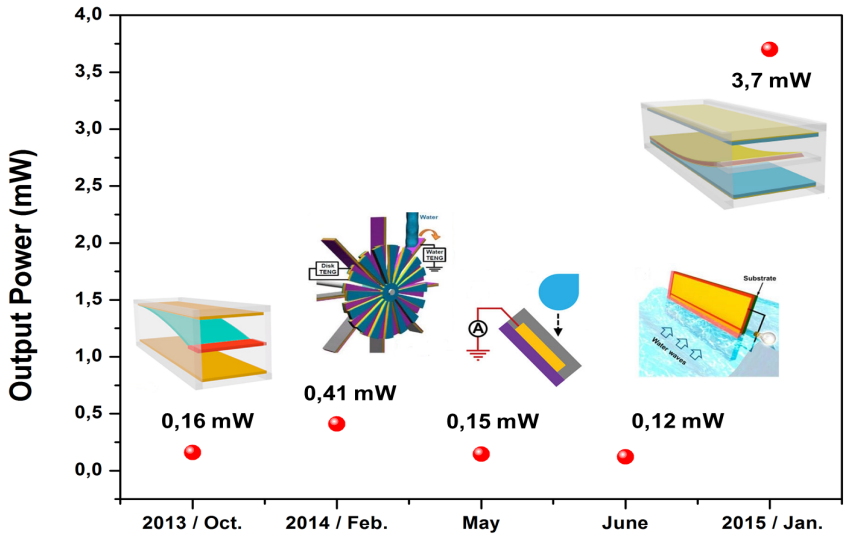

FIGURE 3.1: A summary on the progress made in the output power of TENGs that allow scavenging energy from the motion of fluids [1, 5, 6, 13, 50].

one can envisage a specific design to harvest the mechanical energy of the gas flow to feed wireless sensor nodes.

Triboelectric nanogenerators have high output power, small size, light weight, high energy conversion efficiency (are cost-effective and easy to be scaled up), offer an abundant choice of materials and can interact directly with the water and the wind [51, 52]. However, TENGs are characterized by a high voltage output, but low output current. One way to solve this problem is by designing TENGs in which the total package includes various units to increase the output current. In recent years, research groups have developed triboelectric nanogenerators that harvest energy from the movement of fluids. In Fig. 3.1 we show a brief summary of the evolution of this type of TENGs with reference to its output power. We can observe that, from October 2013 until January 2015, the output power increased by over 20 times.

3.2 Triboelectric Device Evolution and Configuration

We developed a rotary structure triboelectric nanogenerator designed for harvesting small-scale water energy in our normal living environment. Throughout its construction, this device was continuously modified and adapted to operate under increasingly reduced water flows.

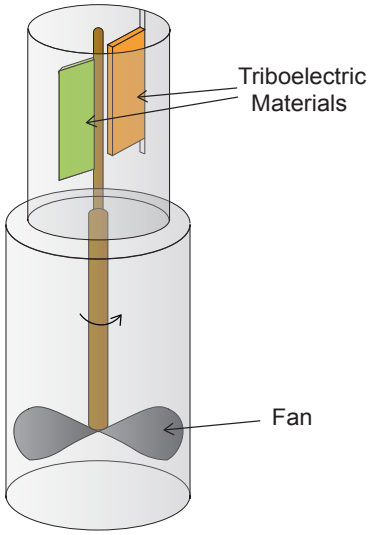

FIGURE 3.2: Basic outline of rotary TENG.

Our goal was to develop a generator with maximum durability, particularly in what regards the triboelectric materials because dust and/or water with different chemical composition can alter the triboelectrification effect and causes a faster wear of materials. On those grounds, the triboelectric materials in our device are isolated, i.e, without direct interaction with water. The motion of water is then just used to rotate blades of triboelectric materials. Figure 3.2 shows the basic outline of the envisaged device.

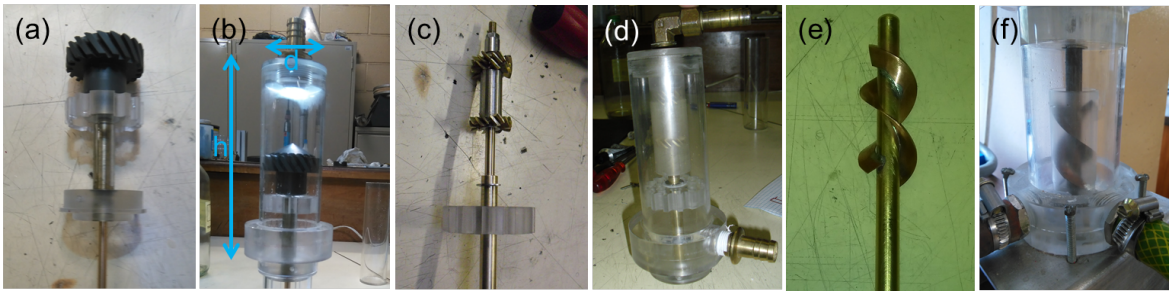

FIGURE 3.3: Evolution stages of the fan for the designed triboelectric generator.

We started by making a fan of PVC (polyvinyl chloride) [Fig. 3.3(a)] with 5.7 cm of diameter and place it in an acrylic tube with a height (h) of 13 cm and a diameter (d) of 6 cm where water flows, as shown in Fig. 3.3(b). Inclined gaps were made to make the fan blades, so that one expected that the water passing through these gaps made the fan rotate. But we observed that, with the designed characteristics, water accumulated inside the tube and the fan rotated only at very high flow rates (above 30 L/min). One possible solution was to reduce the size and weight of the fan [Fig. 3.3(c)] and put it in a smaller tube [Fig. 3.3(d)] so that to water flow was directed and the fan forced to rotate. This new tube has a height of 9 cm and a diameter of 2.5 cm, while the fan dimensions were similar to the previous ones [Fig. 3.3(d)].

In Figs. 3.3(c) and (d) we show the changes performed in the device, but this configuration again did not work as desired. Although it was found that water was better directed inside the small tube, the new configuration of the blades of brass fan weren't appropriate to make then rotate. Some of identified problems included the inclination of the blades, their size and spacing because the water flowed through the blades but did not make them rotated, i.e, they were not appropriate for water flows.

Finally, we made a fan as shown in Fig. 3.3(e) and, with this configuration [Fig. 3.3(f)], we observed that fan rotated as desired for different flow rates. This fan has helical shape and when attached to a support with a rotary plate which comes into contact with the fixed plates used, the fan continues to rotate.

The second step in the construction of the triboelectric generator was the assembly of the triboelectric materials. For this, we developed a system in which the triboelectric material is fixed on a shaft that rotates using the motion of the fan caused by the water flow. Firstly, we

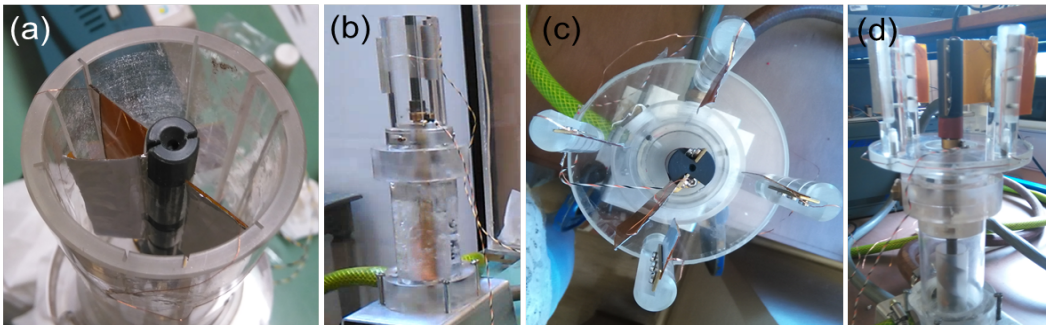

FIGURE 3.4: Evolution of the structure for the assembly of the triboelectric materials.

developed a structure as shown in Figs. 3.4(a) and (b). The structure was composed by an acrylic tube (with a height of 10 cm and a width of 4.9 cm), inside of which gaps were made to fix plates with the triboelectric material. Initially, these gaps were perpendicular to the tube wall but other gaps were subsequently made in a way that the plates are inclined at an angle of approximately 60° in respect to the tube wall. However, we found that, with this configuration, the friction between the plates with the triboelectric material was very large which resulted in a rapid wear. Furthermore, we observed changes in the initial position of the plates fixed to the tube wall because the gaps were not efficient enough to keep the plates completely stable and fixed.

To solve these problems we developed the structure of Figs. 3.4(c) and (d). This new framework had new dimensions (a diameter of 13 cm and 9 cm height brackets for triboelectric materials) with the goal to increase the contact area between the triboelectric materials and obtain higher outputs. This new framework has four brackets to place the triboelectric material, which allows us to use only one, two or four brackets [Figs. 3.5(a), (b) and (c), respectively] and perform a set of systematic studies.

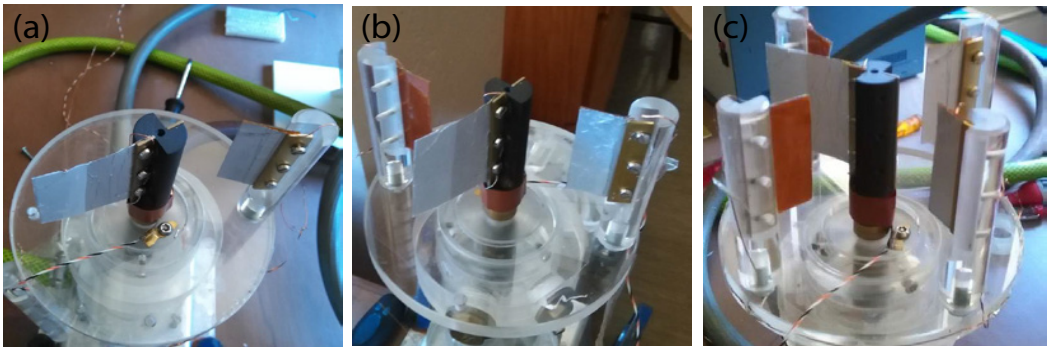

FIGURE 3.5: Final framework with the different configurations for brackets: (a) One bracket; (b) Two brackets; (c) Four brackets.

Initially, the rotating plate was fixed on a shaft [Fig. 3.6(a)] with a diameter of 1 cm and a height of 8.5 cm. However, to improve the fixation we made the changes shown in Fig. 3.6(b) (now having 1.8 cm of diameter and 8.3 cm of height). Although the dimensions are different, they do not interfere with device performance.

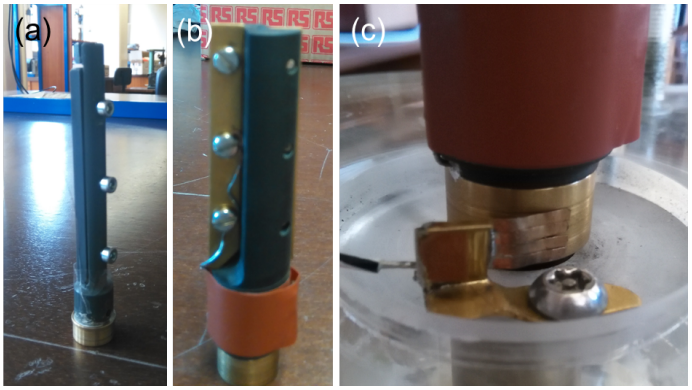

FIGURE 3.6: Alteration of the shaft and brass brush for improved electrical contact.

In this last framework, the electrical contact to the plate was optimized by the use of a brass plate in the shaft, which promotes the conduction of charges from the plate with the triboelectric material to the external circuit. Moreover, a copper brush was made to make electrical contact with the shaft as shown in Fig. 3.6(c).

In Fig. 3.7(a) is shown the schematic of our final device to facilitate a better understanding. The assembled device is shown in the photograph in Fig. 3.7(b).

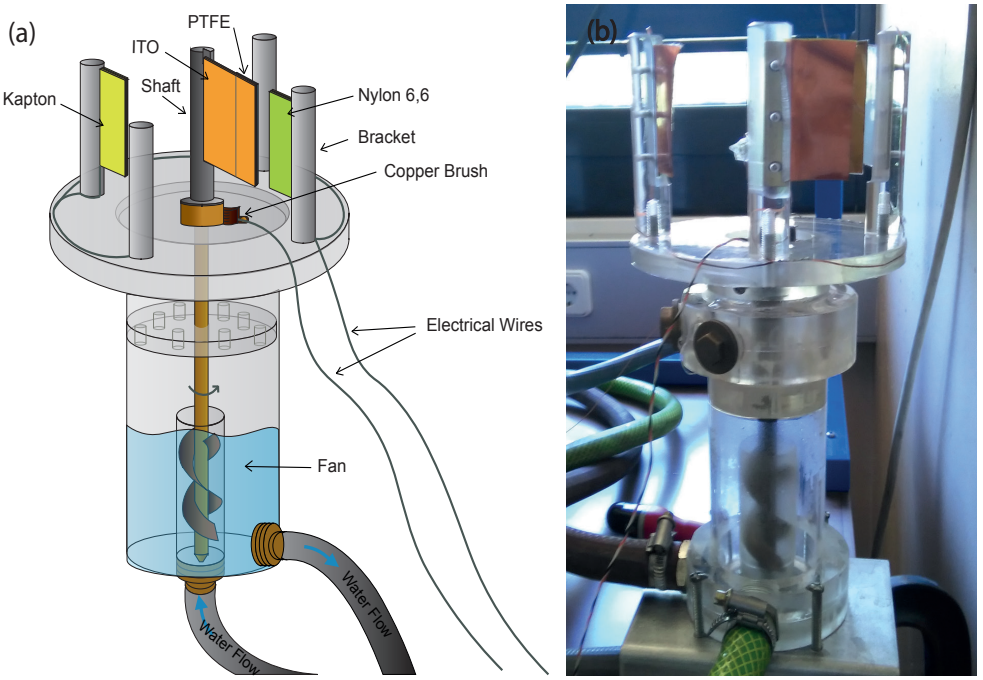

FIGURE 3.7: Device structure of the rotary triboelectric nanogenerator. (a) Schematic diagram and (b) photograph showing the assembled rotary TENG.

When the triboelectric configuration is constituted by two or four brackets, the plates fixed in the brackets can be connected in series or parallel. However, as referred in section 2.2.1, triboelectric nanogenerators have an inherent capacitive behavior. Then, for higher voltage values, the plates placed in the brackets were connected in series. However, if the purpose was to obtain higher currents, these plates have to be placed in parallel.

With small changes in the structure, it is possible to isolate the triboelectric materials and place the device in any environment (water pipelines, taps of housing, etc.) because it was built to function as watertight. This guarantees a greater durability of the material because there is less wear and no influence on the triboelectrification effect by other external agents such as dust.

3.3 Triboelectric Materials and Morphologies of the Surfaces

In this section we will describe the triboelectric materials that we used in our device and mention as we performed the surface texturing in PDMS films using a Si template. Finally, we

describe how to texture the surface of a PDMS film using aluminum foils with ordered hexagonal arrays of pits at its surface due to the self-organized pore formation during the anodization process.

3.3.1 Material Selection and Structural Dimensions

As discussed in section 2.4, it is important to ensure that the two materials that are in contact with each other have opposite triboelectric polarities. For the selection of adequate triboelectric materials, we have consulted a triboelectric series, such as that shown in Fig. 1.2 (section 1.2.1). According to the range of materials that we had available, we chose the PTFE and Nylon 6.6 because they were the two most distant materials in the series, i.e, they have a high charge transfer between them. These two triboelectric materials were used in a film form (thicknesses of 0.05 mm). On one side of the PTFE and Nylon 6.6 films we placed an aluminum foil tape that acts as the electrode.

In our rotary TENG, the plates with the two types of triboelectric materials have different characteristics in relation to its stiffness. Subsequently, in some tests we found that, when the rotating plate [with the PTFE film as shown in Fig. 3.7(a)] and the fixed plate in the bracket are flexible, the contact area is reduced. As a solution, we made the plates stiff but verified that, in this case, contact was also reduced because the rotating plate was very stiff and had contact only in a very small area between the sliding plates. Based on these tests, we made the rotation plate more flexible [as shown in Figs. 3.4(c) and (d)] and found that this would be the best setup, with largest output voltage values.

The plates which are fixed in the brackets are constituted by two sheets (2 cm $\times$ 5 cm) of Kapton (with the function to give stiffness to the plates), a layer of aluminum foil tape (2 cm $\times$ 5 cm) as electrode and a Nylon 6.6 film (1.5 cm $\times$ 5 cm) that is our triboelectric material. Concerning the rotation plate, it is constituted by a sheet (4 cm $\times$ 5 cm) of ITO with 0.1 mm of thickness (making it flexible), with an aluminum sheet (4 cm $\times$ 5 cm) as electrode and a PTFE film (1.5 cm $\times$ 5 cm) as the other triboelectric material.

However, the triboelectric materials used were purchased in the form of film, so that to change their shape, thickness or even to produce microstructures on the in surface is difficult.

Therefore, to make a study of the influence of texture of triboelectric materials on the output voltage, we used PDMS. This is available in solution and can therefore be deposited in thin film form by spinning. As observed in the triboelectric series [Fig. 1.2 (Section 1.2.1)], PDMS is the most negative triboelectric material immediately after PTFE.

3.3.2 Manufacturing process of microstructured PDMS films using a mold

To make a film of PDMS we used Dow Corning's Sylgard 182 elastomer kit which both the PDMS base and the curing agent as part of it. Initially, we placed 0.210 g of the curing agent onto a clear container on an electronic scale and added 2.067 g of PDMS base (i.e. $\sim$ 10 times the weight of the curing agent [53–55])

Subsequently, we mixed this with a spatula (about 10 mins of whisking) to make sure that the curing agent is uniformly distributed. However, we observed that the final mixture is filled with air bubbles from the whisking process [Fig. 3.8(a)], and these bubbles needed to be removed before curing. To make the trapped air bubbles escape, we placed the mixture in a dessicator connected to a vacuum pump for about 1 hour [Fig. 3.8(b)].

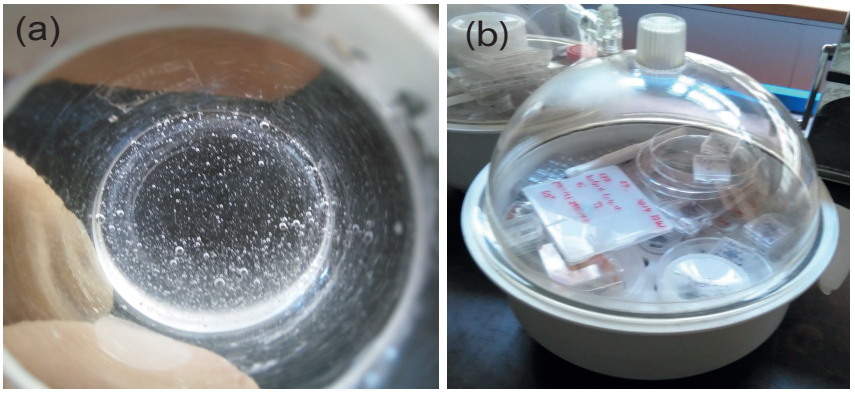

FIGURE 3.8: (a) PDMS mixture with air bubbles; (b) Dessicator used to remove air bubbles from the PDMS.

Once a clear, bubble free PDMS mixture was obtained, the next step was to spin it over a silicon template with pyramid microstructures. This mold was fabricated using optical lithography and chemical etching processes at INESC-MN, Lisbon. We chose this template with pyramids pattern because, as mentioned in section 2.4, a study by F. R. Fan *et al.* showed that

this micropattern type allows the largest increase of the electrical output performance compared with the non-structured films and guarantees high uniformity. For this purpose, we used the spinner in the lithography bay in the clean room.

The **spin-coating deposition technique** is one of the most used methods for thin film fabrication on flat substrates making use of the centrifugal force of the spinning substrate to spread and uniformly coat its surface. The thickness of the thin films is controlled with precision attending to the viscosity and concentration of the solution and the rotation speed of the spinner with increasing angular speed leading to thinner films [56].

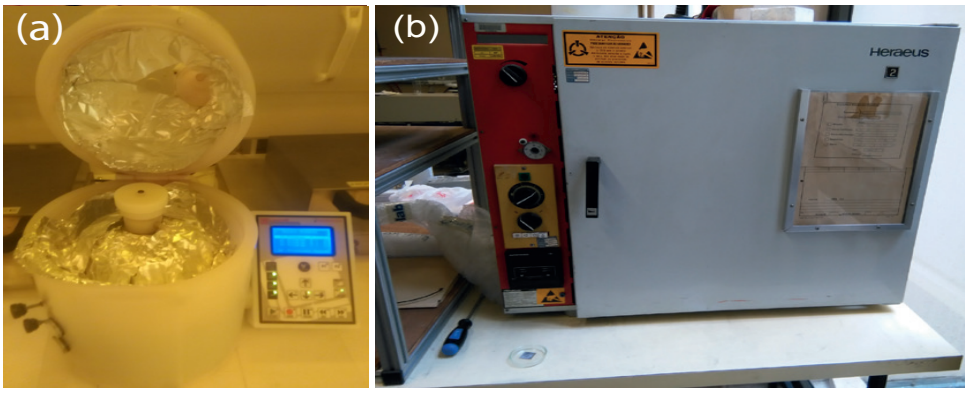

FIGURE 3.9: (a) Laurell WS-650S spinner; (b) Oven for curing PDMS.

Figure 3.9(a) represents the typical spin-coating deposition process. A Laurell WS-650S-6NPP spinner (CEMUP-MNTEC) [Fig. 3.9(a)] was used to spin-coating a PDMS solution on the microstructured Si template using a one step process at 500 rpm for 30 s. To increase the thickness of the PDMS film, the solution was poured again on the template and again spinned, at 900 rpm for 30 s.

After making the deposition of the PDMS film in the Si template, we performed the PDMS cure by placing the film and template on a oven at $80\,^{\circ}\mathrm{C}$ [Fig. 3.9(b)] for 2 hours. All this process is shown diagrammatically in Fig. 3.10.

Finally, we waited for the PDMS to return to room temperature and, placing aluminum foil tape on the obtained template, it was possible to peel it off. This allowed us to obtain a textured PDMS film having patterned the inverse of the original features on the surface of the template (Fig. 3.11). The aluminum foil will then be used as the electrode.

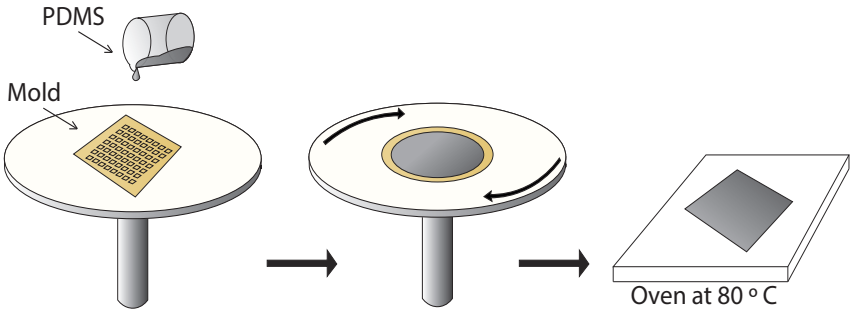

FIGURE 3.10: Spin-coating deposition process.

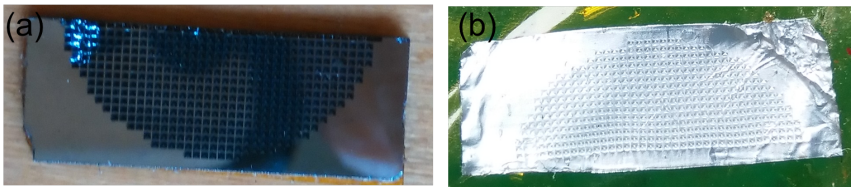

FIGURE 3.11: (a) Silicon template with pyramid microstructures; (b) Textured PDMS film having patterned the inverse of the original features.

However, the overall area of this Si template was much smaller than the dimensions of the plates with triboelectric material used in our device. Therefore, our aim was only to achieve the texturing of the surface of PDMS and test its influence when compared to the non-structured surface. For such a systematic testing, a system was developed by Carla Alves under her Master's thesis this allowed us to estimate the output values if the textured surface had the dimensions of the triboelectric plates (1.5 cm $\times$ 5 cm).

3.3.3 Texturing surfaces using aluminum foils with ordered hexagonal arrays of pits

Another strategy that was followed to obtain textured PDMS film was to use self-organized porous anodic aluminum oxide (AAO) [57].

Prior to anodization, we cleaned the Al (99.999 % purity) substrates in acetone and ethanol using an ultrasonic bath for 3 min. Additionally the Al substrate was electropolished [as illustrated in Fig. 3.12(b)] in 25 % of percloric acid ($HClO_4$) and 75 % of ethanol (C_2H_5OH) by

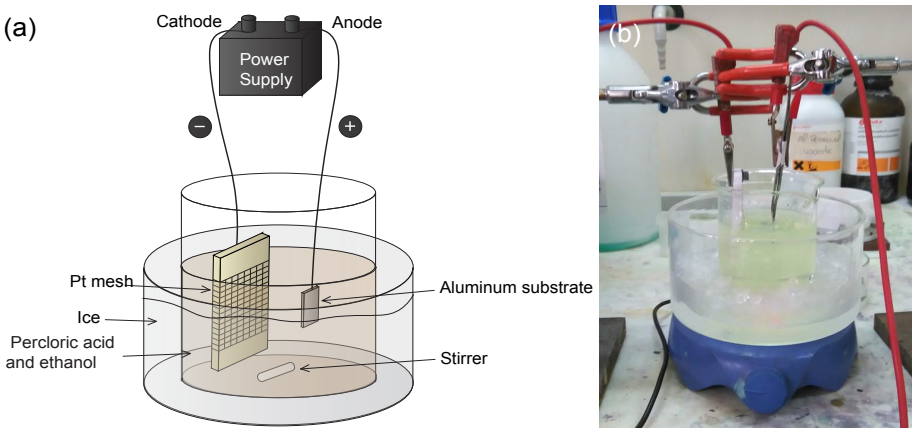

FIGURE 3.12: (a) Representation (adapted from [58]) and (b) the two electrodes on setup used for electropolishing.

applying 20 V between the Al substrate (anode) and a Pt mesh (cathode) for 2 min with the solution below $10\,^{\circ}\mathrm{C}$ (experimental temperature was $7.3\,^{\circ}\mathrm{C}$). This leads to the smoothnening of the Al surface [59].

The next step was the anodization process. An anodized aluminum layer grows under a constant potential applied between the Al foil (anode) and a Pt mesh (cathode) in an electrochemical cell containing an acid electrolyte (Fig 3.13).

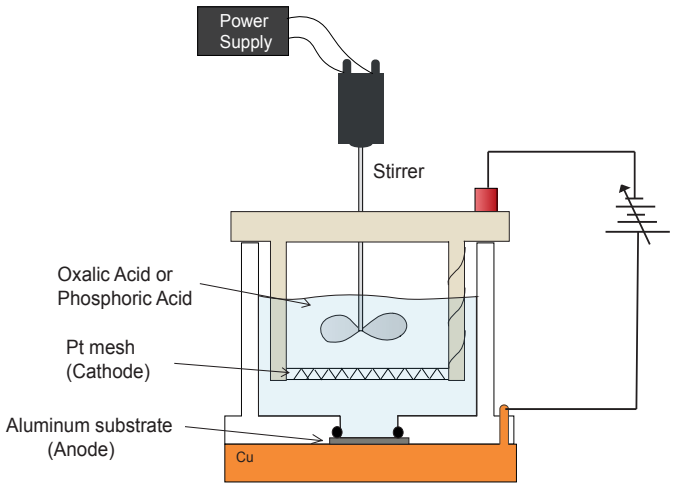

FIGURE 3.13: Representation of the experimental setup used for the anodization process.

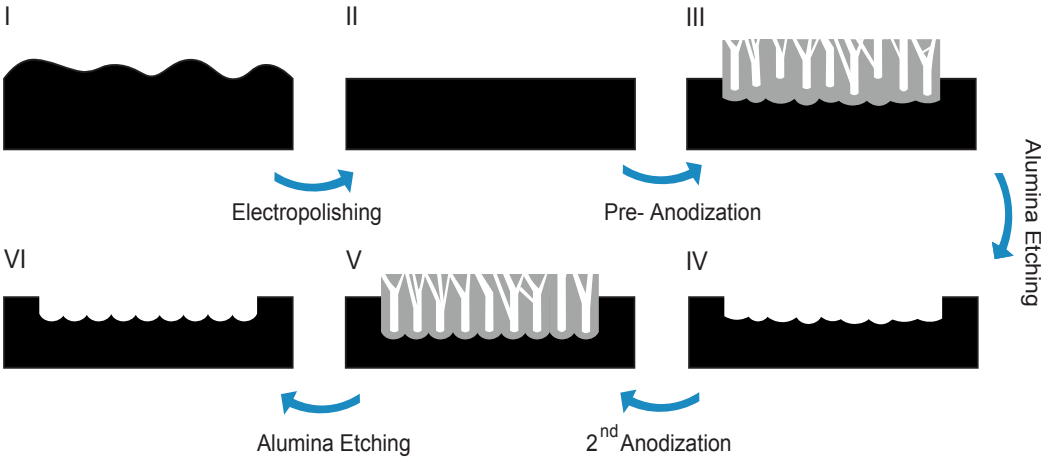

FIGURE 3.14: Representative scheme of the fabrication process of an Al foil with ordered hexagonal arrays of pits using electrochemical anodization.

Initially, we made a pre-anodization with oxalic acid ($C_2O_4H_2$, 0.3 M) by applying 40 V during 8 min, at an experimental temperature of $5.1\,^{\circ}\mathrm{C}$. During the pre-anodization, the pores nucleate randomly at the aluminum surface (step III in Fig. 3.14) and, after a certain time, the mechanical tension induced by neighboring pores initiates a self-assembling of the pore [59]. Basically, this anodizing is softer and create pores randomly in order to be easier phosphoric acid anodized aluminum.

To significantly improve the results, we carried out a chemical removal (H_3PO_4 and H_2CrO_4) of the alumina layer already with the nanoporous structure during 5 min at a temperature of $70\,^{\circ}\mathrm{C}$ in agitation. This process was then followed by a new anodization. The small cavities of the aluminum film originated in the previous pores (step IV in Fig. 3.14) will lead to more organized and aligned, and with a better defined structure (step V in Fig. 3.14) due to the pattern of organized cavities that were already created. The pre-anodization was made with phosphoric acid (H_3PO_4, 0.1 M) by applying 195 V during 12 hours at an experimental temperature of $1.7\,^{\circ}\mathrm{C}$. Table 3.1 summarizes the various anodization parameters implemented for the acids used in the two anodization processes.

As we want the aluminum foils with ordered hexagonal arrays of pits at their surface, due to the self-organized pore formation, we removed the alumina layer formed in the second

TABLE 3.1: Anodization parameters.

Electrolyte	Concentration (M)	Potential (V)	Temperature ($^\circ$C)	Anodization Rate μm h^{-1}
$C_2O_4H_2$	0.3	40	2 - 6	$\sim$ 2.5
H_3PO_4	0.1	195	1 - 2	$\sim$ 5

anodization by a chemical etching process (H_3PO_4 and H_2CrO_4) for 6 h at $40\,^\circ$C in agitation (step VI in Fig. 3.14).

According to the available setup, the aluminum samples had a diameter of 1 cm. Comparing this dimension with the dimensions of the plates used in the rotary TENG, again it was not possible to cover the whole area of our plates using the microstructured PDMS using our aluminum template. Nevertheless, the objective of this process was to prove that it is possible to texture PDMS films using the ordered hexagonal arrays of pits at the aluminum surface.

This method has the advantage of being very fast and low cost, when compared to the production of the Si template in the previous section and it is possible to reuse the same template and texture the surface of other polymers.

After the aluminum molds were made, we performed the same procedure as in section 3.3.2, replacing the Si template by the aluminum mold.

Chapter 4

Automated Measurement Device

After the production of our rotary TENG, an important parte of the developed work consisted in the creation of a systematic testing method capable of acquiring reliable and repeatable data to evaluate the performance of our TENG. In this chapter we explore all the devices developed and used to measure the electrical outputs of our TENG. For this, a circuit board was developed for to study the output characteristics under different load resistances.

4.1 Schematics and Assembly

Our TENG harvests energy from the water flow and to make the different studies, we constructed a closed circuit for the recirculation of water. To regulate the water flow for the different studies, a water pump, to which was connected one acrylic flowmeter, was used. This allowed us to control and measure the water flow.

The electrical outputs of our TENG was obtained by connecting our device to a circuit board with a wide range of resistances. The circuit of each resistance is controlled by relays, wherein each realy is controlled by an Arduino using LabVIEW. The relays are powered by a voltage source. An oscilloscope [60] (connected to the computer using a GPIB-USB converter [61]) and controlled by a LaVIEW program, was used to acquire the electrical outputs. Finally a low-noise preamplifier [62] was connected to the oscilloscope for the current measurements.

The components used during this thesis to study the performance of our rotary TENG are illustrated in Fig. 4.1.

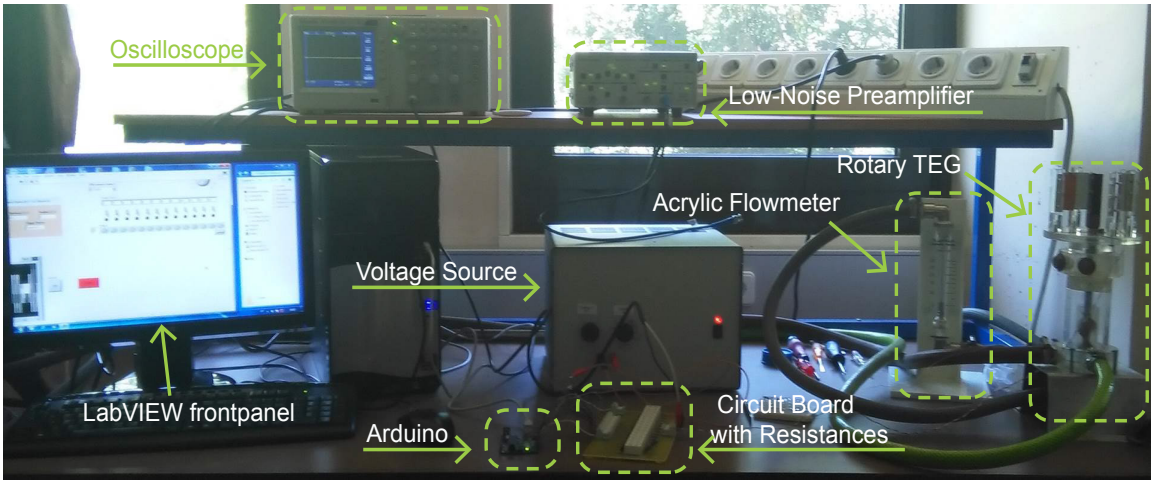

FIGURE 4.1: Elements of the automatic measuring device and rotary TENG.

4.2 Voltage and Current Measurements

4.2.1 Oscilloscope Acquisition

To evaluate the performance of the fabricated TENG we developed an acquisition system to measure the generated voltage and current. For this, a Tektronix TDS 1002C-EDU oscilloscope [60] was used. In channel 1 we acquired the open-circuit voltage, while channel 2 was used to acquire the short-circuit voltage that allowed us to calculate the short-circuit current.

During the acquisition of the voltage, a voltage divider [Fig. 4.2(a)] was required to collect the data obtained by the oscilloscope. This was necessary because, for high voltage values (exceeding 50 V), the oscilloscope acquisition window was not sufficient to achieve a complete acquisition of the data. The used voltage divider reduced to half the voltage values obtained [Fig. 4.2(b)]. For this we used two resistances (R_1 and R_2) with a value of $1M\Omega$ and considering that V_{out}=$\frac{R_2}{R_1+R_2}V_{in}$, one has $V_{out} = \frac{1}{2}V_{in}$, as intended.

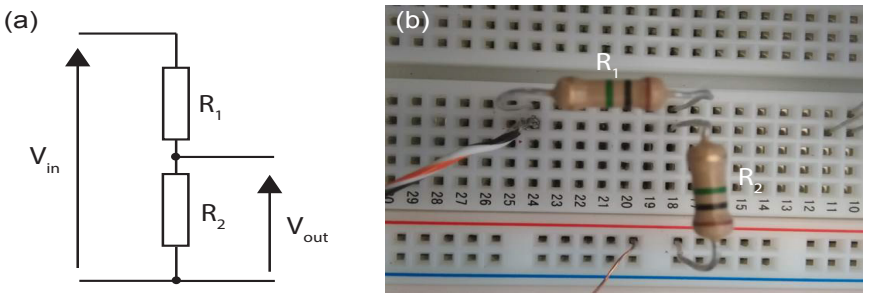

FIGURE 4.2: The voltage divider used to collect the data obtained by the oscilloscope.

To measure the short-circuit current of our device, we measured the voltage drop on a resistance of (10.1 $\pm$ 0.1) Ω with the oscilloscope connected to the low-noise preamplifier. Measuring the tension drop value (V) and knowing the resistance value (R), we then determined the value of the short-circuit current using Ohm's law.

4.2.2 Low-Noise Preamplifier

The SR560 Low Noise Preamplifier [62] was used to amplify the small voltage peaks obtained in the oscilloscope and thus determine the current. This device was configured on its front panel to obtain in the oscilloscope the cleanest possible signal. For this purpose, we configured the SR560 Low Noise Preamplifier with a high-pass filter at + 6 dB/octave and a low-pass filter at + 6 dB/octave, and cutoff frequencies of 300 Hz and 1 KHz, respectively.

Considering the gain settings available and the experimental tests performed to determine the minimum value for the necessary gain, the instrument's gain was set to 100.

4.2.3 Circuit Board with Resistances

To study and estimate the output characteristics under different load resistances, we developed one circuit board with a range of resistances ranging from 10 Ω to 10 GΩ [Fig. 4.3]. When the TENG is connected to an arbitrary resistor, the output properties can be estimated and, thus, determined the maximum power for each configuration and water flow. However, the resistance of 10 Ω could not be used because the resistance common to the whole circuit has of the same order of magnitude. Therefore, we started taking the voltage and current values

for resistances larger than 10 Ω. This way, we were able to determine the current and voltage values and obtain the resistance which gives the optimum output power.

The circuit board was made with the EAGLE program, which allowed us to create the circuit to be printed. Then, the circuit was printed by using photo-sensitive printing and two chemical solutions (caustic soda and iron perchlorate). Finally, all electronic components are soldered to the board with the printed circuit.

The circuit board was prepared for 15 resistances [(10.0 $\pm$ 0.5) Ω, (100 $\pm$ 5) Ω, (1.00 $\pm$ 0.05) kΩ, (10.0 $\pm$ 0.5) kΩ, (100 $\pm$ 5) kΩ, (1.00 $\pm$ 0.05) MΩ, (10.0 $\pm$ 0.5) MΩ, (47.0 $\pm$ 2.4) MΩ, (68.0 $\pm$ 0.2) MΩ, (82.0 $\pm$ 8.2) MΩ, (100 $\pm$ 1.0) MΩ, (470.0 $\pm$ 23.5) MΩ, (1.0 $\pm$ 0.1) GΩ, (5.0 $\pm$ 0.3) GΩ and (10 $\pm$ 0.5) GΩ], although the resistance of 10 GΩ was not placed on the board due to its dimension [Fig. 4.3(a)]. However, the range of available resistances was sufficient and there was no need for the 10 GΩ resistance. To automatically select each resistance, 15 relays were used.

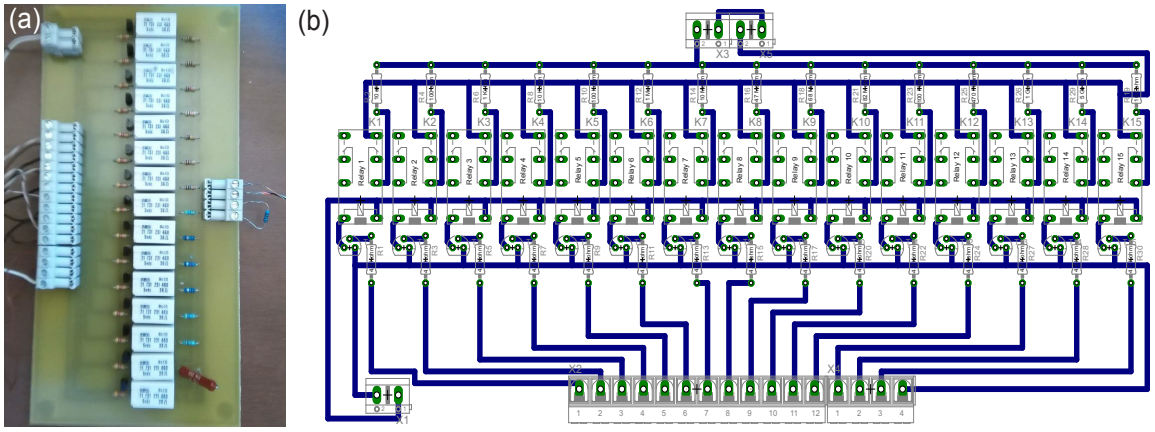

FIGURE 4.3: Circuit board with a wide range of resistances: (a) Photograph of the developed circuit board; (b) Printed circuit form.

A relay is an electrically operated switch. Each relay is supplied with 6 V using an external voltage supply (with complete electrical isolation between control and controlled circuits). The control and choice of relay is performed using an Arduino UNO [63] controlled by a LabVIEW program. This connection was performed using the LabVIEW Interface for Arduino Uno. Thus, the automatized acquisition of the current and voltage values for each resistance was possible. The LabVIEW program used for the data acquisition by the oscilloscope was

developed by Carla Alves under her Master's thesis and the LabVIEW frontpanel used is illustrated in Fig. 4.4.

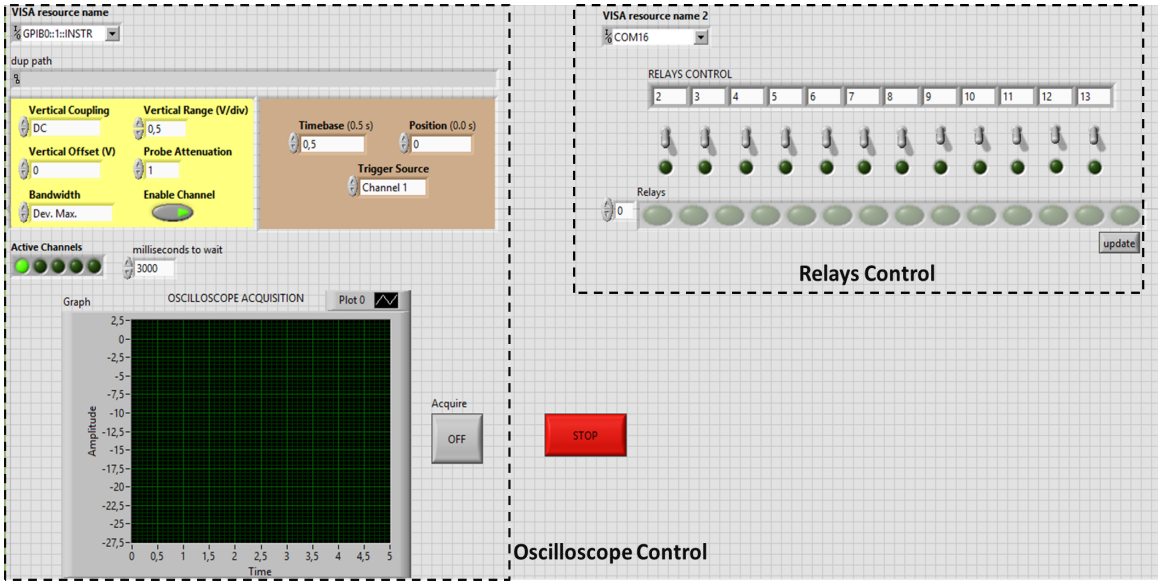

FIGURE 4.4: LabVIEW frontpanel developed for relays control and oscilloscope acquisition.

4.3 Frequency Measurements

Another important parameter to study the performance of our device was the rotating frequencies of our TENG for different water flows and for the different triboelectric configurations. To determine the rotating frequencies we used a reed switch [Fig. 4.5(a)]. The reed

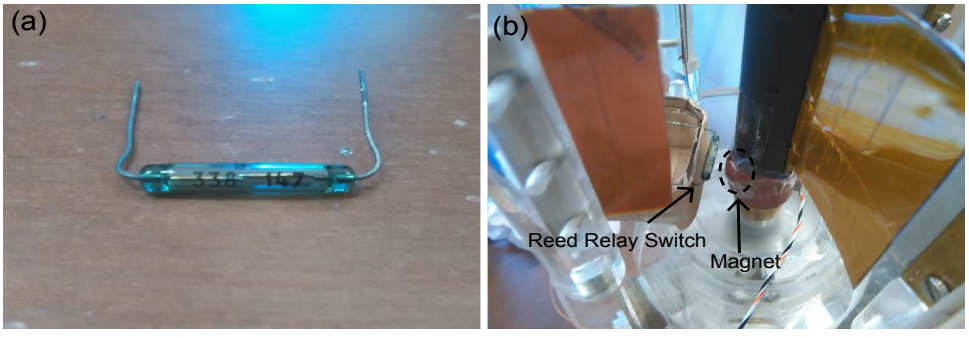

FIGURE 4.5: (a) Reed Switch used; (b) Position of the reed switch and of the magnet in our rotary TENG for the determination of the rotating frequency.

switch is an electrical switch that uses magnetic fields. This relay is constituted by a pair of contacts on ferrous metal reeds in a hermetically sealed glass envelope.

Initially, the contacts are opened. When a magnetic field is applied, the reeds come together and close the electrical circuit. When the magnetic field ceases, the stiffness of the reeds causes them to separate and again open the circuit.

For the measurement of the rotating frequencies, the reed switch was fixed in the assembly for the triboelectric materials and the magnet was placed on the shaft that will rotate with different frequencies, as shown in Fig. 4.5(b). After that, the reed switch was fed by a 5 V voltage source and its signal obtained by the oscilloscope [60].

Chapter 5

Results and Discussion

This chapter presents the obtained results and their subsequent discussion. In the first section we describe the results obtained in this work with the materials used and reported in section 3.3.1. We analyse the results of different configurations (with one PTFE plate and one Nylon plate, one PTFE plate and two Nylon plates or one PTFE plate and four Nylon plates). Using the developed measurement setup, we measured the open-circuit voltage and the short-circuit current. The second section describes the analysis of the results when using an non-structured PDMS film and its comparison with a PDMS film with a structured surface (patterns of pyramids and ordered hexagonal arrays of pits). The last section describes the physics behind the electrical generation process of our rotary triboelectric device, including a detailed account of each step involved during the operation.

5.1 Performance Analysis of the Device

After producing our rotary TENG and creating a systematic testing method capable of investigating the performance of TENGs, we systematically measured electric output of our device. As mentioned in section 3.2, our rotary TENG has four brackets with Nylon plates. Initially, we used only one bracket (with Nylon plate) and a rotating plate (PTFE plate), both with non-structured surfaces.

5.1.1 One Nylon Plate

To investigate the relationships between the open-circuit voltage (V_{OC}) and water flow, a systematic measurement was performed under different water flows (20, 22.5, 25, 27.5 and 30 L/min). The experimental results are shown in Fig. 5.1. First graph [Fig. 5.1(a)] corresponds to

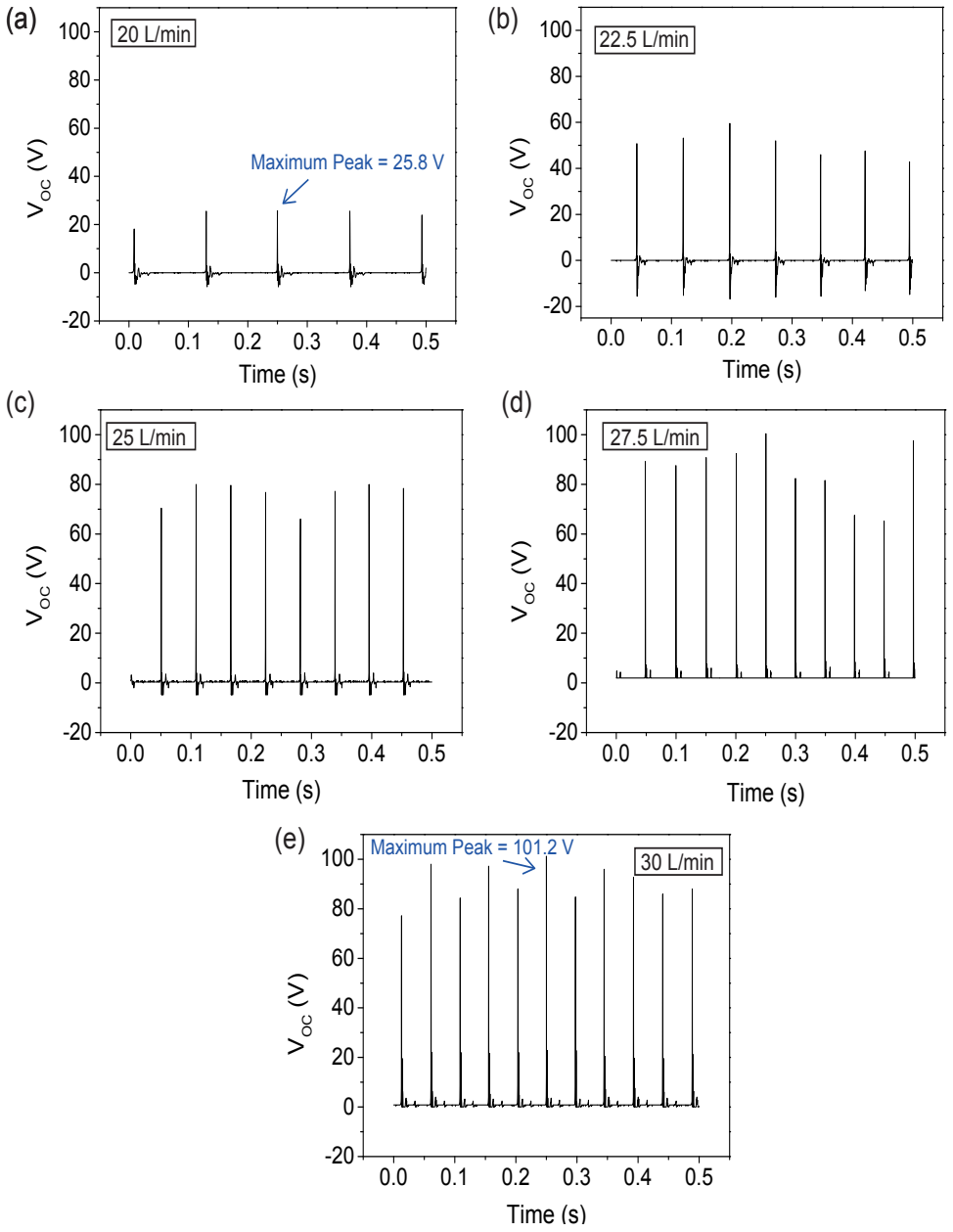

FIGURE 5.1: Open-circuit voltage peaks of the rotary TENG with one Nylon plate and one PTFE plate for different water flows: (a) 20; (b) 22.5; (c) 25; (d) 27.5; (e) 30 L/min.

20 L/min, wherein the voltage peaks appear when there is contact between the plates. However, the value of all peaks under the same water flow is not constant and, therefore, we consider the mean value. We also observe that, for each acquisition there is a maximum value, and for 20 L/min was 25.8 V. Analyzing and comparing the graphs of Fig. 5.1 we find that the maximum of V_{OC} occurs at 30 L/min and the maximum open-circuit voltage peak is 101.2 V.

Figure 5.2(a) shows the influence of the water flow on the open-circuit voltage, showing an increase of the mean value of the V_{OC} peaks with increasing water flow. The maximum of

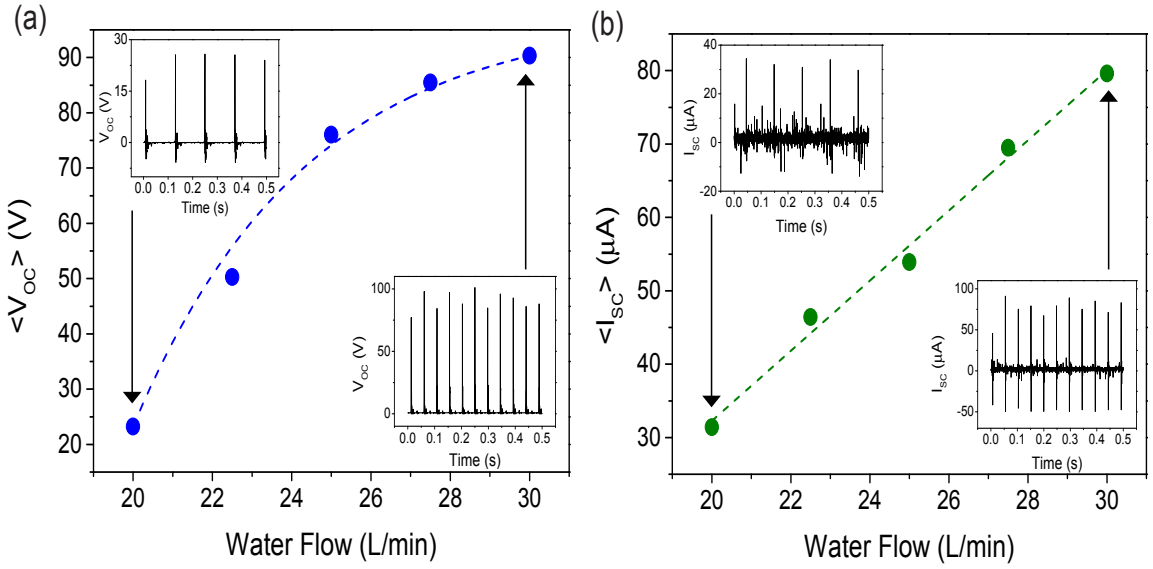

FIGURE 5.2: Influence of the water flow on the (a) mean open-circuit voltage and the (b) mean short-circuit current for rotary TENG with one Nylon plate and one PTFE plate.

V_{OC} occurs at 30 L/min, where the mean value of the voltage peaks is $\sim$ 90.3 V. However, for low water flows (20 L/min), the mean V_{OC} is $\sim$ 23.2 V, while the maximum V_{OC} peak is of 25.8 V. Accordingly, there is an influence of the water flow on the generated open-circuit voltage, with

TABLE 5.1: Mean short-circuit currents for the different water flows for the device with Nylon and PTFE plates.

Water Flow (L/min)	$< I_{SC} >$ (μA)
20	$\sim$ 31.4
22.5	$\sim$ 46.4
25	$\sim$ 53.9
27.5	$\sim$ 69.5
30	$\sim$ 79.6

an increasing trend of the values of the voltage peaks with increasing water flow. This trend can be explained by changes in the generated surface charge density. The higher the rotation speed, the larger will be the contacting force between the polymer films. The larger contacting force will make the two surfaces contact more intimately, resulting in a higher surface charge density.

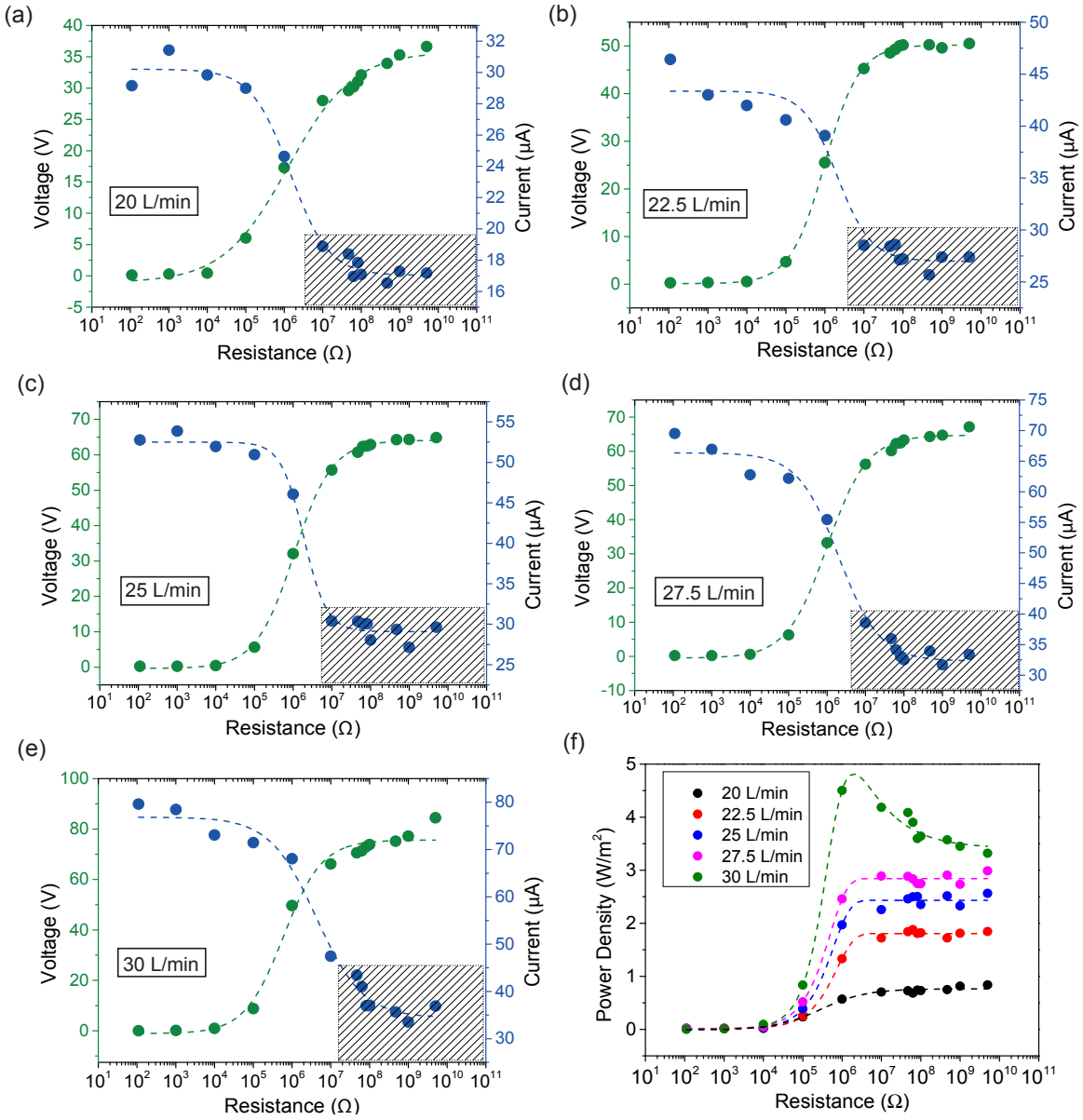

FIGURE 5.3: The output voltage, current and the power density of the rotary TENG with one Nylon plate and one PTFE plate, driven by different water flows.

Figure 5.2(b) shows the influence of the water flow on the mean short-circuit current ($< I_{SC} >$), showing an increase of the current with increasing water flow. Table 5.1 is a summary of the mean short-circuit current values obtained for all water flows measured. We found that, when the water flow rate is 30 L/min, the mean current is $\sim$ 79.6 μA. This value is higher compared to the other water flows and tends to decrease as the flow of water also decreases, reaching a mean current of $\sim$ 31.4 μA for 20 L/min. There is also an increasing tendency of the I_{SC} peaks with the increase of the water flow due to the increased amount of transferred charges.

To further investigate the performance of our rotary TENG, we measured its electric output when connected to variable load resistances, ranging from 100 Ω to 5 GΩ. The electrical outputs obtained for the different water flows are illustrated in Fig. 5.3. In all cases we found that the voltage of the circuit increases with increasing load resistance, while the current has the reverse trend.

In theory, we would expect that the current would go to zero for high load resistance values. However, during the study of the short-circuit current we found that, for the higher resistances, the measured current never reached zero and the value that we obtained was approximately equal to that of the open-circuit noise.

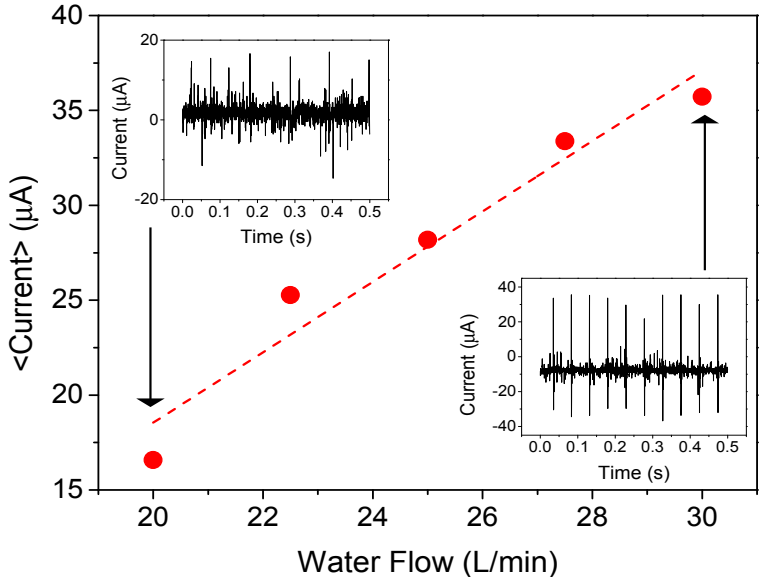

FIGURE 5.4: Dependence of noise of rotary TENG with the different water flows.

After some tests, whose purpose was to reduce this noise, we found a tendency of increasing noise with increasing water flow, as shown in Fig. 5.4. Thus, we concluded that this noise did not originate for the measuring apparatus, but from our device itself. For this reason, the shaded area in the graphs of Figs. 5.3(a) to (e) correspond to the range of values that we believe is within the noise level of our measurements and it should not be taken into account in the data analysis.

Analysing Fig. 5.3(f), we found that the maximum power density occurs between the range of resistances from 1 MΩ to 10 MΩ for all flow rates studied and, in case of water flow of 30 L/min the value is $\sim$ 4.5 W/m^2.

To find the optimized number of brackets in the rotary TENG structure for the most effective electricity generation, we also investigated the performance of our device with 2 and 4 brackets (with two and four Nylon plates, respectively) as comparisons. The obtained results will be present in the next sections.

5.1.2 Two Nylon Plates

In this section we will study the performance of our rotary TENG with two Nylon plates in brackets and a PTFE plate (rotational plate) as the triboelectric configuration of the device. We again performed a systematic study, to obtain the relation of open-circuit voltage (V_{OC}) as a function on the variation of the water flow, as shown in Fig. 5.5(a).

We observed that the voltage increases with the increase of the water flow, showing a mean value $\sim$ 69.6 V and a maximum peak of 80.0 V for 30 L/min. However, in comparison with the device configuration used in section 5.1.1, the obtained V_{OC} is lower. The probable reason for this is related with the increased number of brackets with Nylon plates. By increasing the number of brackets, there will be less space in between them and the contact-separation processes will occur with a larger frequency. However, the rotating plate (with PTFE) will have less space to recover its original shape from the bending state after sliding each bracket. Consequently, the effective contact area between the Nylon and the PTFE surfaces will be reduced.

Figure 5.5(b) shows the influence of the water flow on $< I_{SC} >$, showing an increase of current with increasing water flow. Table 5.2 is a summary of the obtained $< I_{SC} >$ for the

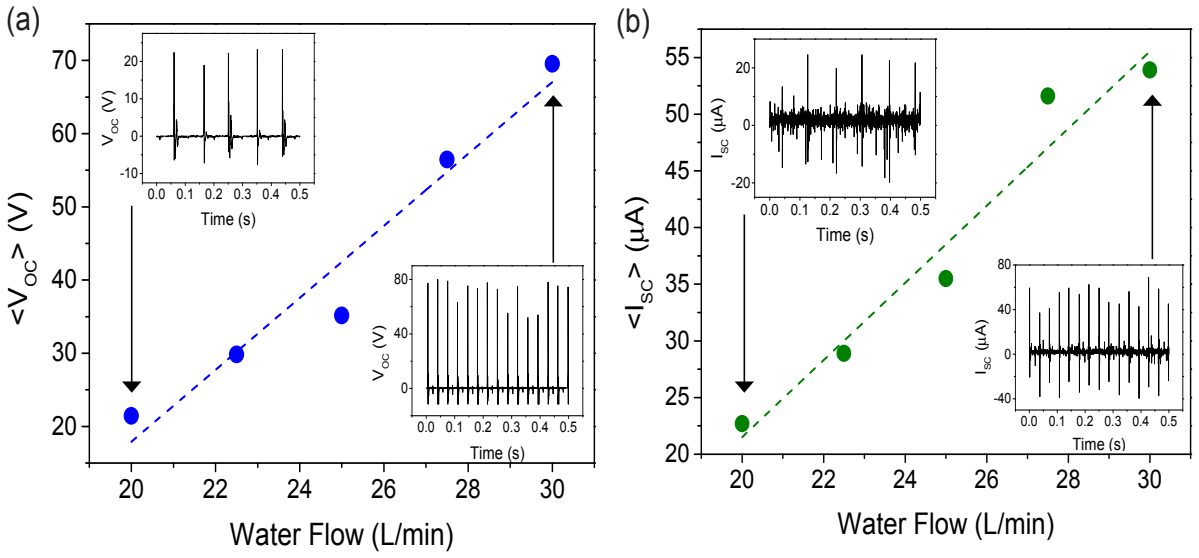

FIGURE 5.5: Influence of the water flow on the (a) open-circuit voltage and the (b) short-circuit current for rotary TENG with two Nylon plate and one PTFE plate.

different water flows analyzed. For a flow rate of 30 L/min, we obtained $< I_{SC} > \sim 53.9$ μA, which is the higher value when compared to the others water flow. In fact, I_{SC} decreases with decreasing water flow, reaching a mean current of ~ 22.7 μA for 20 L/min.

TABLE 5.2: Mean short-circuit currents for the different water flows for device configuration with two Nylon plates and one PTFE plate.

Water Flow (L/min)	$< I_{SC} >$ (μA)
20	$\sim$ 22.7
22.5	$\sim$ 28.9
25	$\sim$ 35.5
27.5	$\sim$ 51.6
30	$\sim$ 53.9

When our rotary TENG was connected to variable load resistances (ranging from 100 Ω to 5 GΩ), we again measured the voltage and I_{SC}. Figure 5.6 shows these electrical outputs for the different water flow that were investigated. As previously seen in section 5.1.1, here we also found that the voltage of the circuit increases with increasing load and the current has the reverse trend. For high resistances, the voltage is higher and this value tends to increase for higher water flows, as demonstrated by comparing the graphs from Figs. 5.6(a) to (e).

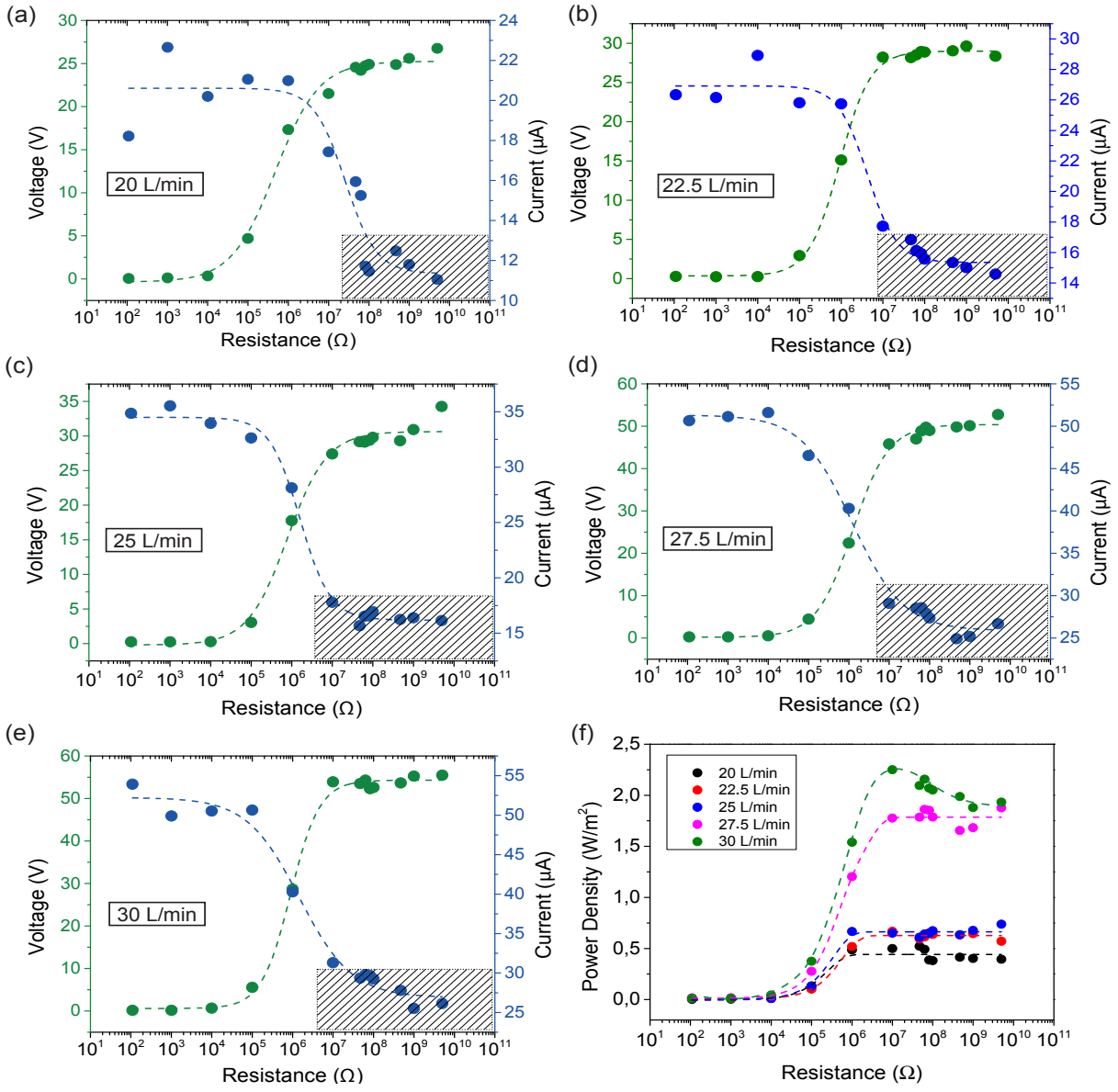

FIGURE 5.6: The output voltage, current and the power density of the rotary TENG with two Nylon plates and one PTFE plate, driven by different water flows.

Again, we expected the current to go to zero for high load resistances. Therefore, the relatively large current for high resistance are depicted as a shaded area in the graphs of Figs. 5.6(a) to (e), as it is related to the noise of our experiments. The noise is represented in Fig. 5.7, where we found that it tends to increase with the increase of the water flow.

Analysing Fig. 5.6(f), we found that the maximum power density for the water flow of 20 L/min, 22.5 L/min and 25 L/min occurs between the range of resistances from 1 MΩ to 10

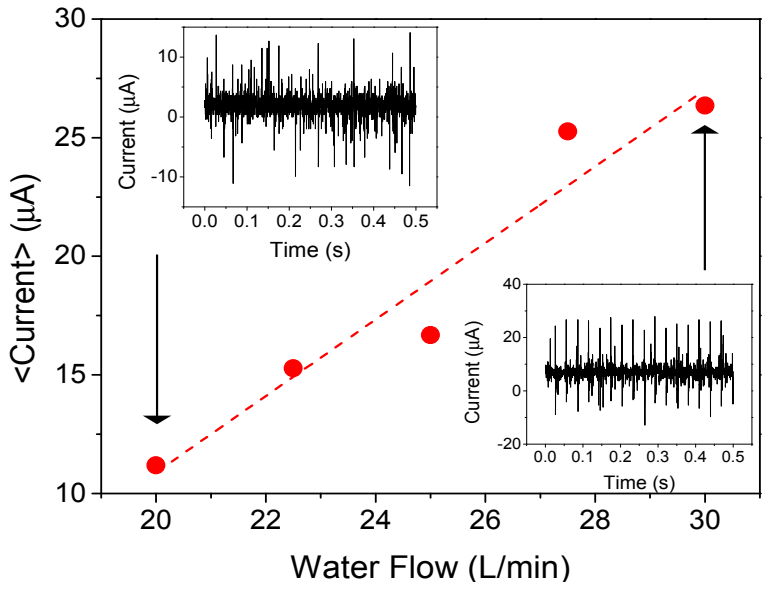

FIGURE 5.7: Dependence of noise of rotary TENG with the different water flows.

MΩ, while for 27.5 L/min and 30 L/min it occurs between 1 MΩ and 47 MΩ. The power density has a maximum value of approximately 2.3 W/m^2 for this triboelectric configuration when the water flow is 30 L/min.

5.1.3 Four Nylon Plates

In this section, we will examine the performance of our device when its triboelectric configuration is constituted by four Nylon plates in the brackets and one PTFE plate (rotating plate). Our study with varying water flow reveled that V_{OC} increases with increasing water flow [Fig. 5.8(a)], with the maximum V_{OC} occurring for a water flow of 30 L/min (as in the previous configurations). For 30 L/min, the mean of the open-circuit voltage peaks is approximately 75.3 V and the value of the maximum V_{OC} peak is 90.8 V. However, for 20 L/min the mean V_{OC} is $\sim$ 21.7 V, while the maximum V_{OC} peak is of 27.2 V.

Relatively to the short-circuit current, Fig. 5.8(b) shows that I_{SC} increases with increasing of the water flow and Table 5.3 summarizes the $< I_{SC} >$ values for all water flow analyzed. For a flow rate of 30 L/min, $< I_{SC} >$ reaches $\sim$ 77.7 μA and decreases with decreasing water flow, reaching $\sim$ 26.0 μA for 20 L/min.

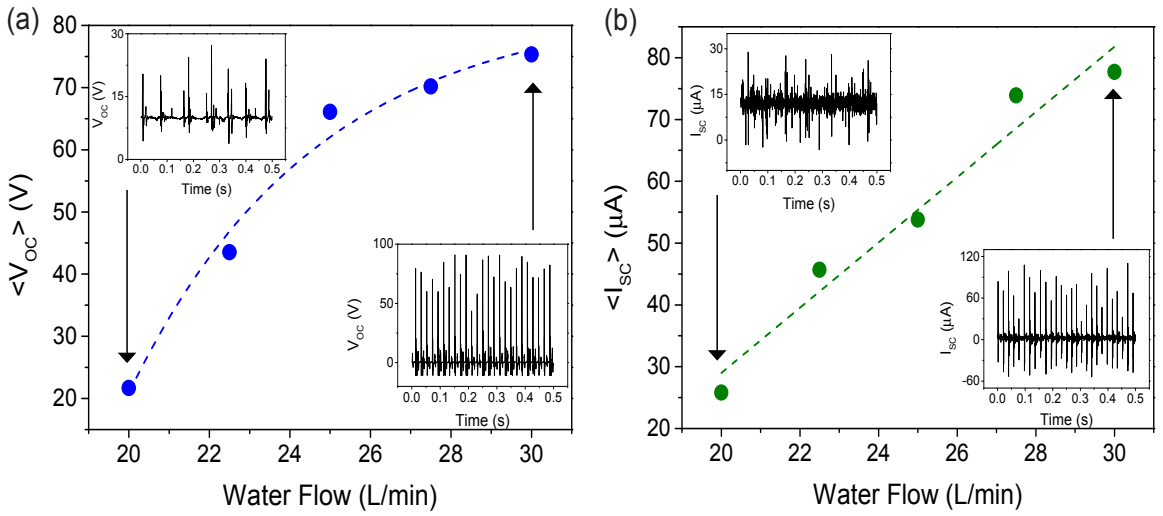

FIGURE 5.8: Influence of the water flow on the (a) open-circuit voltage and the (b) short-circuit current for rotary TENG with four Nylon plate and one PTFE plate.

TABLE 5.3: Mean short-circuit currents for the different water flows for a device configuration with four Nylon plates and one PTFE plate.

Water Flow (L/min)	$< I_{SC} >$ (μA)
20	$\sim$ 26.0
22.5	$\sim$ 45.7
25	$\sim$ 53.8
27.5	$\sim$ 73.9
30	$\sim$ 77.7

The electrical outputs as a function of the load resistance obtained for each water flow are represented in Figs. 5.9(a) to (e), where, for all the different flow rates, the voltage of the circuit increases with the increase of the load and, again, I_{SC} has the reverse trend. Analysing Fig. 5.9(f), we found that the maximum power density for the water flow of 20, 22.5, 25, 27.5 and 30 L/min occurs between the range of resistances from 1 MΩ to 47 MΩ. For this device configuration, the power density has the maximum value for 30 L/min, reaching approximately 4.1 W/m^2.

The shaded areas in the graphs of Fig. 5.9 again correspond to the noise caused by our device and should not be taken into account. In Fig. 5.10 is represented the dependence of the noise with the variations of the water flow, revealing that this configuration produces the highest noise in the experimental data.

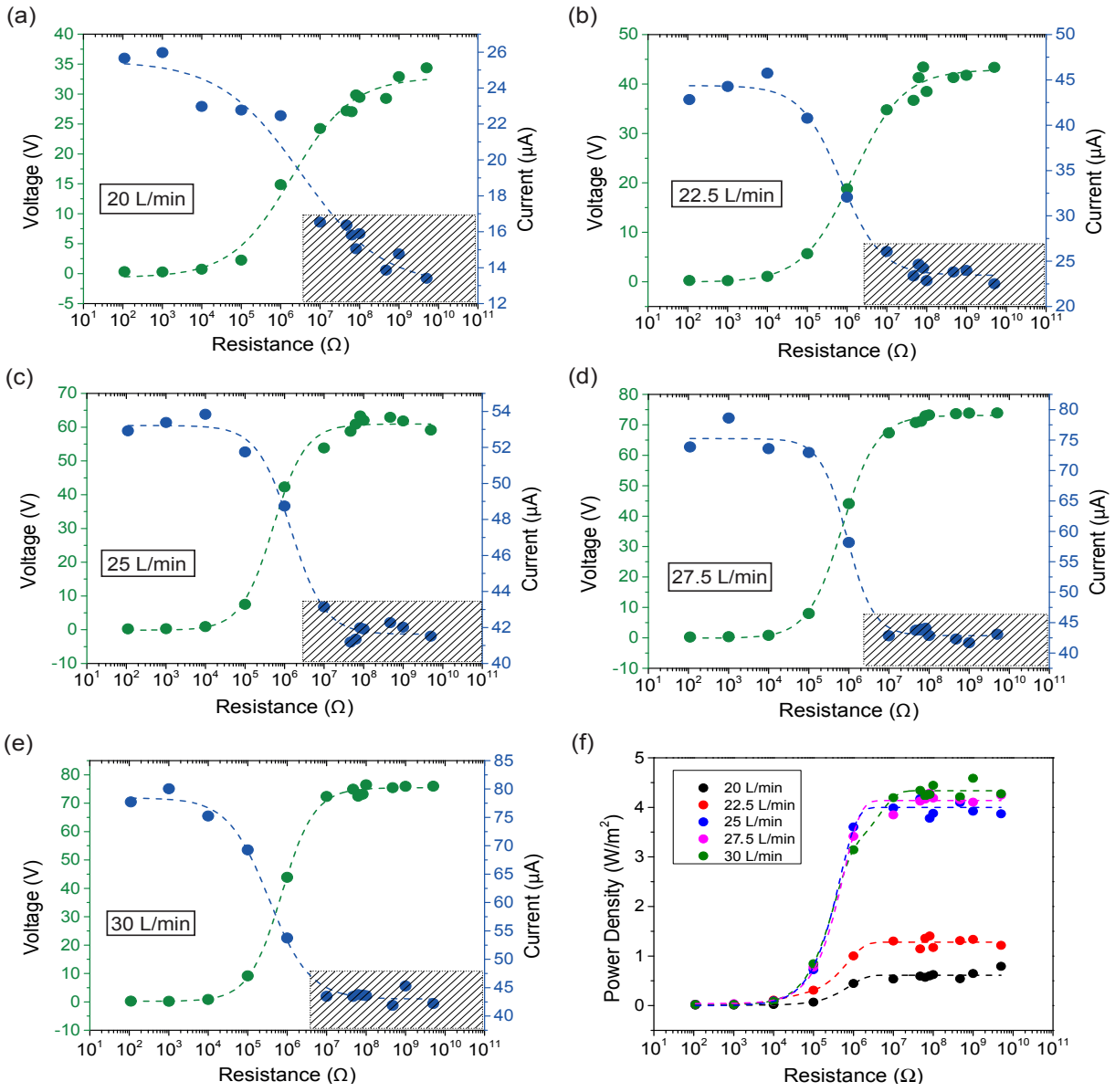

FIGURE 5.9: The output voltage, current and the power density of the rotary TENG with four Nylon plates and one PTFE plate, driven by different water flows.

5.1.4 Final Discussion

Figure 5.11 summarizes the influence of the water flow on $< V_{OC} >$ and $< I_{SC} >$, and the variation of the frequency of the rotation plate with the water flow for different triboelectric configurations.

Comparing the configuration constituted by four Nylon plates and one PTFE plate with

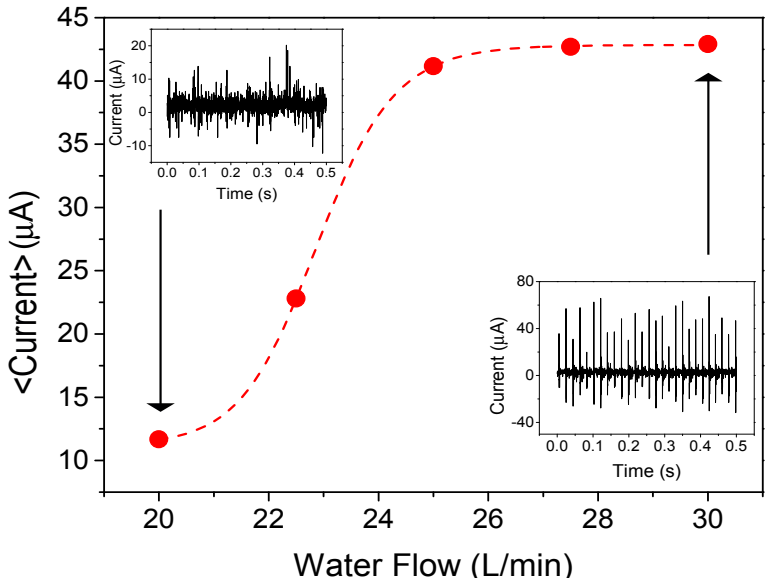

FIGURE 5.10: Dependence of noise of rotary TENG with the different water flows.

the configuration of one Nylon plate and one PTFE plate [Fig. 5.11(a)], the obtained $< V_{OC} >$ is lower. The probable reason for this is the increased number of brackets with Nylon plates, as mentioned in section 5.1.2.

However, the $< V_{OC} >$ for the triboelectric configuration with four Nylon plates is higher than with two Nylon plates [Fig. 5.11(a)]. The reasons for this results can be related with variations in the plate positions, small changes in the dimensions or in the manufacture of the plates and/or degradation of the plates.

Figure 5.11(b) shows that $< I_{SC} >$ increases with increasing water flow to all triboelectric configurations. The configurations with one and four Nylon plates practically obtain the same short-circuit current values for different water flows. However, the triboelectric configuration constituted by two Nylon plates and one PTFE plate, gave the lowest short-circuit current.

The maximum power density for the three different configurations, under various water flows, is shown in Fig. 5.11(c). We observe that P_{max} increases with increasing water flow to all cases. However, the configurations with one and four Nylon plates have values of P_{max} highest than with two Nylon plates and one plate PTFE.

To the three studied configurations, we saw that the largest electrical output takes place for 30 L/min. To determine which configuration is the best structure for the effective energy

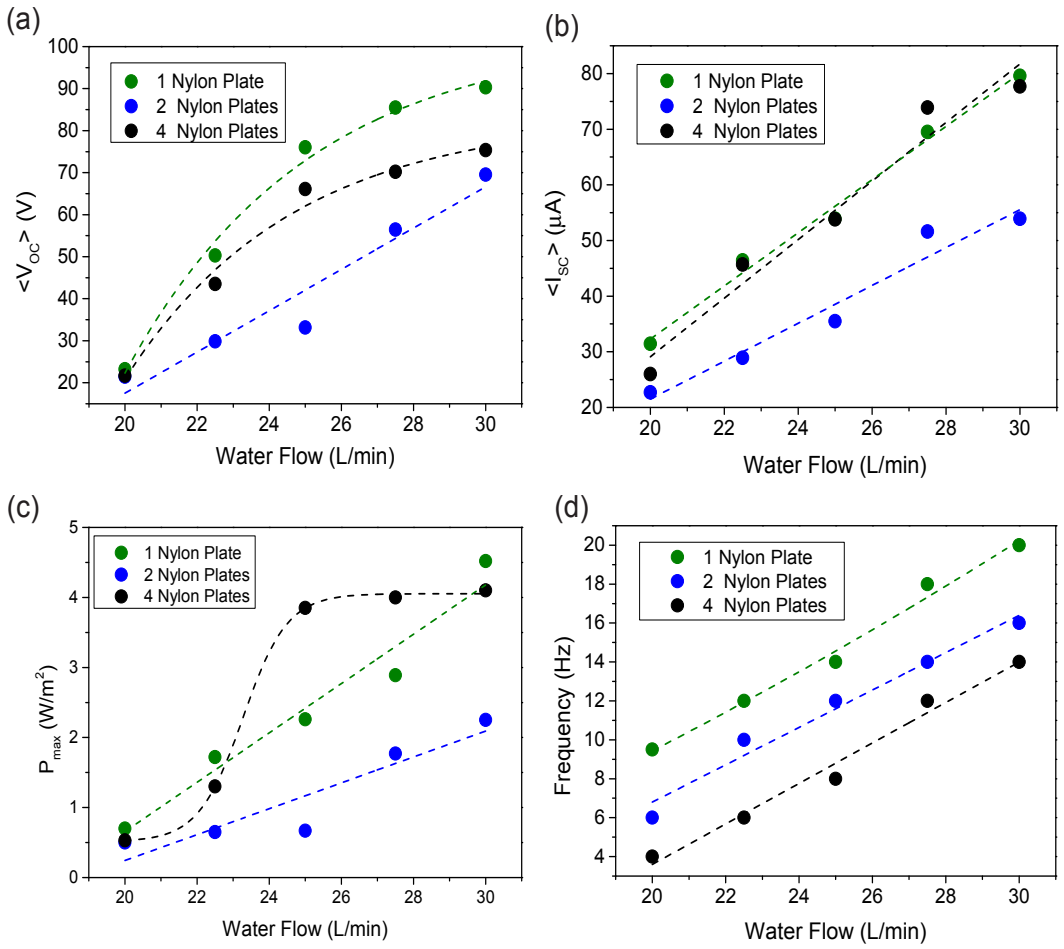

FIGURE 5.11: (a) Summary of the influence of the water flow on (a) $< V_{OC} >$, (b) $< I_{SC} >$ and (c) maximum power density. (d) Variation of the frequency of the rotation plate with the water flow for different triboelectric configurations.

harvesting through water movement, we calculated for each one the power per second (P_s) and per cycle (P_{1cicle}). In Table 5.4 we summarize the results obtained for each configuration. We

TABLE 5.4: Power per second and power per cycle for the water flow of 30 L/min for three different triboelectric configurations.

	1 Nylon Plate	2 Nylon Plates	4 Nylon Plates
P_s (mW/s)	$\sim$ 66.8	$\sim$ 49.5	$\sim$ 153.7
P_{1cicle} (mW/cycle)	$\sim$ 3.3	$\sim$ 3.1	$\sim$ 11.0

can see that the configuration of four Nylon plates gives P_s = 153.7 mW/s and P_{1cicle} = 11.0 mW/cycle, one Nylon plate one has P_s = 66.8 mW/s and P_{1cicle} = 3.3 mW/cycle and for the two Nylon plates, P_s = 49.5 mW/s and P_{1cicle} = 3.1 mW/cycle. We conclude that the four Nylon

plates configuration optimizes the performance of the device, allowing the largest power to be reached.

Figure 5.11(d) shows the rotating frequency of the plate for the three triboelectric configurations, revealing a linear increasing trend. As expected, the frequency is higher when our device is constituted by one Nylon plate only.

Lastly, using our device with its triboelectric configuration constituted by a Nylon plate and a PTFE plate, more than 50 serial-connected commercial LEDs were lit up using a flow of 30 L/min from the rotary TENG, as shown in Fig. 5.12. Note that, due to the fact that the LEDs (Light Emitting Diodes) were not positioned at the same angle, it gives the wrong illusion that they are not all light up [Figs. 5.12(b) and (c)].

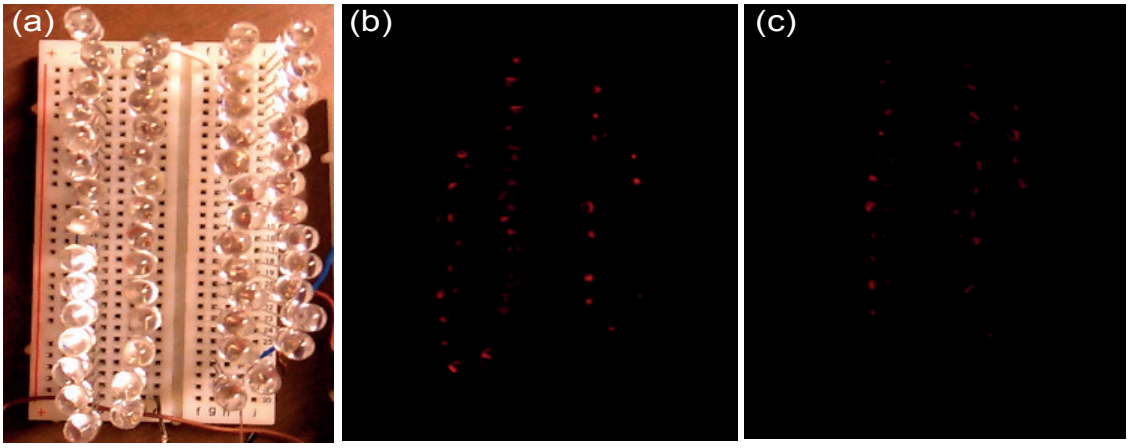

FIGURE 5.12: Set of LEDs used to test the performance of the rotary TENG: (a) LEDs off; (b) and (c) LEDs lit up.

Comparing with the different triboelectric nanogenerators mentioned in the literature, particularly those developed by Dr. Z. L. Wang's group, we have seen that ever since the first realization of a TENG in January 2012 (with a power density $\sim$ 3.7 mW/m^2) the output power density of TENG was improved by five orders of magnitude within 12 months (to a power density $\sim$ 313 W/m^2) [3]. One of the last TENGs was developed by Tang *et al.* and was based on a liquid-metal-based triboelectric nanogenerator for high power generation [7]. In this case, for contact area of 15 cm^2, the device reaches a voltage of 679 V, a current of 9 μA and a power density of 6.7 W/m^2. More importantly, the instantaneous energy conversion efficiency was demonstrated to be as high as 70.6 $\%$ [7]. In our case, the maximum power obtained is 3.4

mW. When compared with Fig. 3.1 (section 3.1), we observe that this value is approximately equal to the output power obtained for one of the latest TENGs that allow scavenging energy from the motion of fluids.

5.2 Influence of Surface Morphology on the Performance of the Rotary TENG

Since triboelectrification is a surface charging effect, we performed the surface texturing PDMS films using a Si mold with patterned micro-pyramid and an aluminum foil with ordered hexagonal arrays of pits (nanoscale pattern). The goal was to increase the effective friction area between structured PDMS films and the Nylon film, and thus the triboelectric effect. For this, we used a system developed by Carla Alves under her Master's thesis for a systematic testing.

To study and compare the influence of texturing the PDMS surface (with Si and aluminum templates) with respect to a non-structured film, we used the same contact surface area ($\sim$ 0.75 cm ^{2}) between the PDMS and the Nylon films.

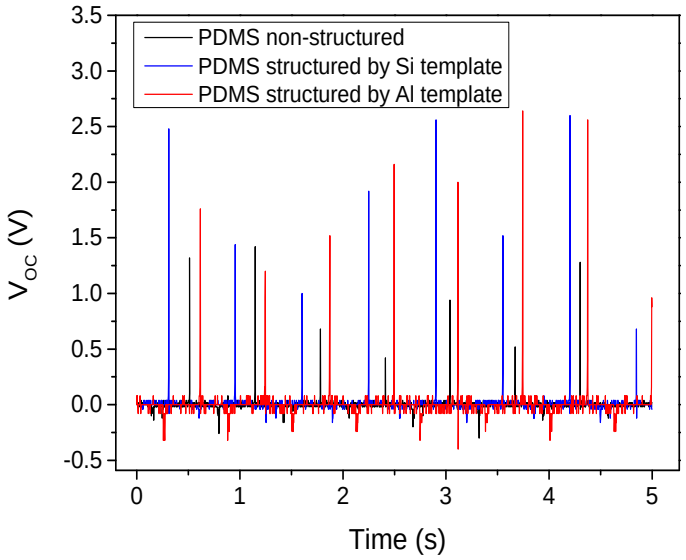

FIGURE 5.13: Output voltage of a TENG using PDMS thin film with non-structured and structured (pyramid/aluminum templates) surface.

Through this systematic testing we compared the output voltage between the non-structured surface and structured surfaces of PDMS films, when in contact with Nylon film.

Figure 5.13 shows the open-circuit voltage obtained for each case. Through the analysis of these V_{OC} peaks, we determined the mean (maximum) voltages of $\sim$ 0.9 V (1.4 V), $\sim$ 1.8 V (2.6 V) and $\sim$ 1.9 V (2.6 V) for the non-structured, micro-pyramids and nano-pits PDMS films, respectively. Therefore, the two patterns allow led to approximately the same result. For PDMS film non-structured, the mean value of the voltage peaks is $\sim$ 0.9 V and the maximum V_{OC} peak is 1.4 V.

We can conclude that with the texturization of the surface of the PDMS film by the two methods used, there is an increase of the effective friction area, and thus of the triboelectric effect. This increase was reflected in a doubling of the mean value of the voltage peaks. Therefore, it is expected that, when we replace the PTFE plate (1.5 cm $\times$ 5 cm) used in our rotary TENG, by a textured PDMS plate with the same dimensions, we should also obtain a 2$\times$ increase of the output voltage in respect to the results obtained in the previous sections.

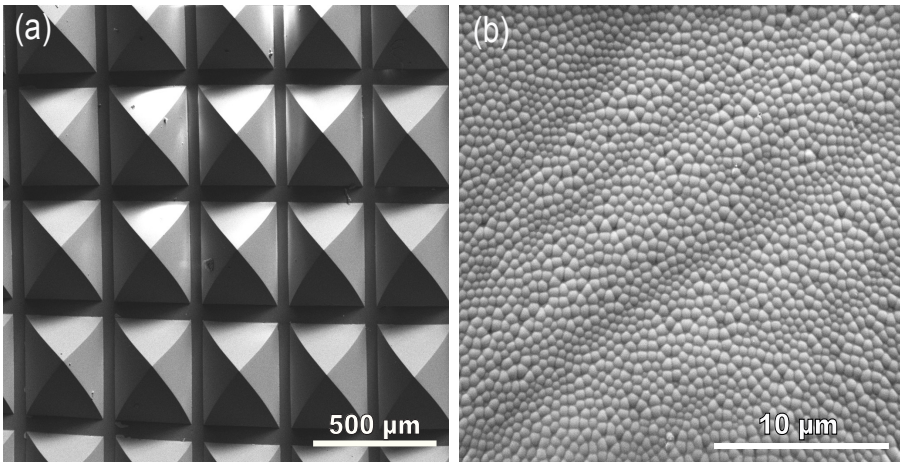

FIGURE 5.14: SEM images of surface texturing of PDMS films with (a) micro-pyramids and (b) nano-pits patterns.

In order to verify the surface texturization of the PDMS films by both methods, a Scanning Electron Microscope (SEM) was used. **Scanning Electron Microscopy** is a morphological characterization technique which retrieves information from the sample's surface and all the SEM images were obtained with the high resolution FEI Quanta 400FEG scanning electron microscope (CEMUP-MNTEC). Figure 5.14 shows the SEM images of the textured surfaces of

PDMS films. For the surface texturing PDMS film with micro-pyramids pattern [Fig. 5.14(a)], we observed that each pyramid has a base length of approximately 333 μm and the pattern is perfectly uniform. For the aluminum template method, we obtained the expected PDMS film with a nano-pits pattern [Fig. 5.14(b)] where $\sim$ 450 nm is the mean diameter of nano-pits.

To increase the friction area and the efficiency in the power generation process of the device it is important that the pyramid features have a perfect geometric structure and a sharp tip. On the other hand, it is also necessary to study the dimensions of the micro- and nano-structures on the surfaces of triboelectric materials that allow to achieve a high performance of devices.

5.3 Working Mechanism of Rotary TENG

Figure 5.15 schematically represents the step-by-step working principle of our rotary TENG, which can be explained as a result of triboelectrification and electrostatic induction. Here, the generated electricity results from a hybridization of the contact-sliding-separation-contact processes.

When there is no water flow, the fan is stationary and consequently, the triboelectric layers (PTFE and Nylon 6.6) are separated from each other. This corresponds to the original state as illustrated in Fig. 5.15(a), where there are no tribo-charges on the triboelectric surface. Immediately upon beginning the water flow, the fan and the plate fixed on the shaft start to rotate, bringing the PTFE film into full contact with the Nylon 6.6 on either one of the brackets [Fig. 5.15(b)]. The triboelectric materials in contact have different tribo-polarities (i.e. different tendencies to gain or lose electrons) and the triboelectric effect will enable the generation of surface charges at the contact area (leaving the PTFE with net negative charge and the Nylon 6.6 with positive charge). The contact surfaces have opposite charge with equal densities and a small electric potential difference is generated.

The fan continues to rotate and, since the PTFE plate is flexible, it will bend in order to sweep across the more rigid Nylon plate [Fig. 5.15(c)]. The strong electrostatic attraction between the two tribo-charged surfaces has the tendency to keep the intimate contact between

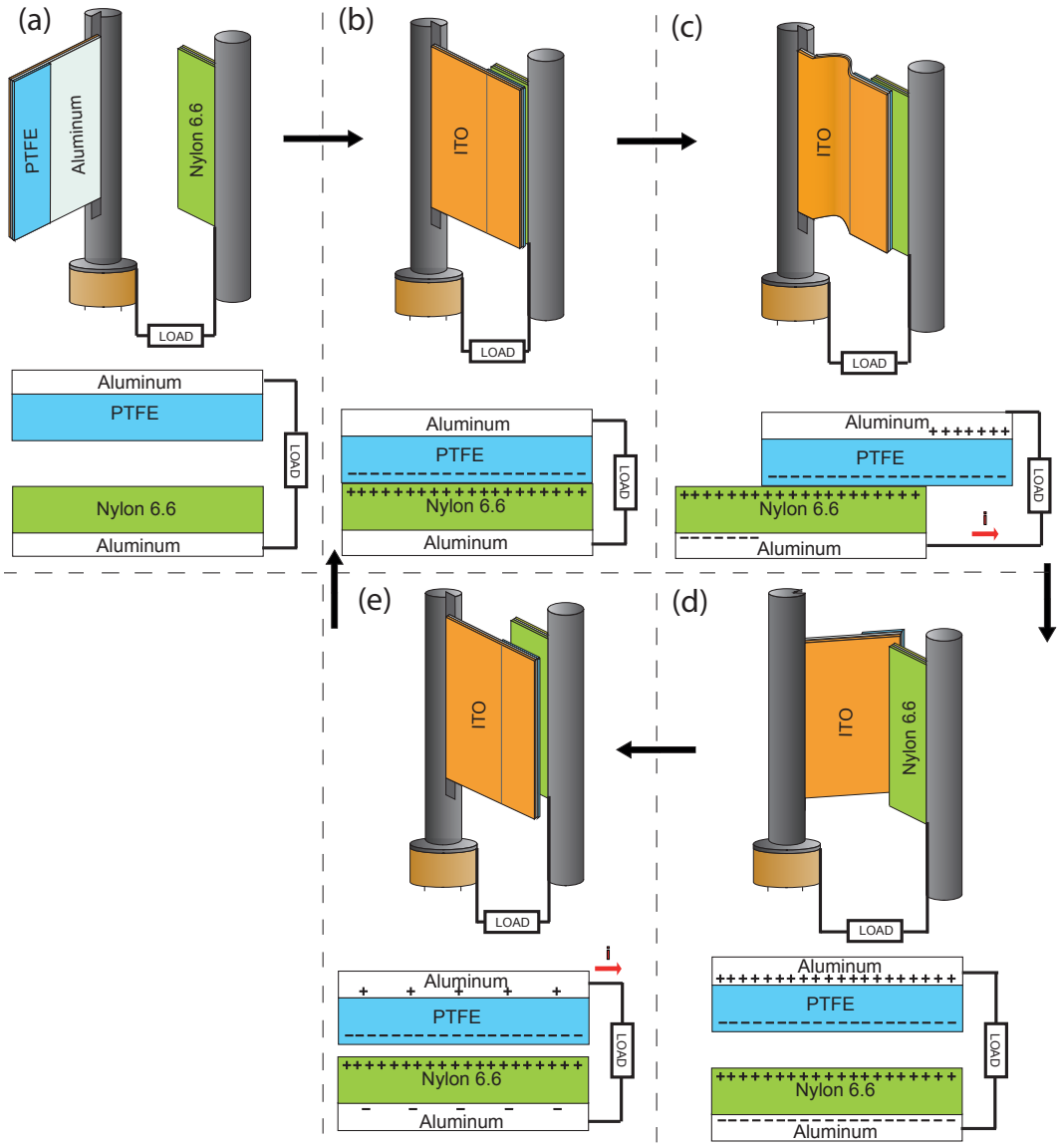

FIGURE 5.15: Device working mechanism of the rotary TENG based on a hybridization of contact-sliding-separation-contact processes. (a) Original position without water flow; (b) PTFE is brought into contact with the Nylon 6.6 layer; (c) PTFE is sliding apart from the Nylon 6.6 surface; (d) PTFE is separated from the Nylon 6.6 layer; (e) PTFE approaching the next Nylon 6.6 material.

the PTFE film and the Nylon plate. With the rotation of the fan, the PTFE plate is guided to slide across the Nylon surface and there is a continuous decrease in the overlapping area between the two triboelectric surfaces.

During sliding, due to the incomplete overlap of the surfaces, a disequilibrium of charges appears and these charges generate an electric field almost parallel to the plates,

inducing a higher potential at the electrode of the Nylon layer. The generated potential difference drives a current flow in the external load from the electrode of the Nylon layer to that of the PTFE layer in order to generate an electric potential drop that cancels the tribo-charge-induced potential. This process will continue until the two triboelectric layers are entirely separated [Fig. 5.15(d)] and the total transferred charges will equal the amount of the triboelectric charges on each surface. This is the sliding mode and it provides much more friction than the contact mode.

With the water flow, the fan will continue to rotate until it arrives to the next bracket with another Nylon plate. When the two triboelectric layers approach, the two surfaces will get into contact momentarily in the vertical direction [Fig. 5.15(e)]. An electric potential difference pointing from the PTFE electrode to the Nylon electrode will be generated, driving a reversal current flow and thus a transference of charges from the PTFE electrode to the Nylon electrode until electrostatic equilibrium is again reached. This is the contact-separation mode and, at this point, a cycle is completed.

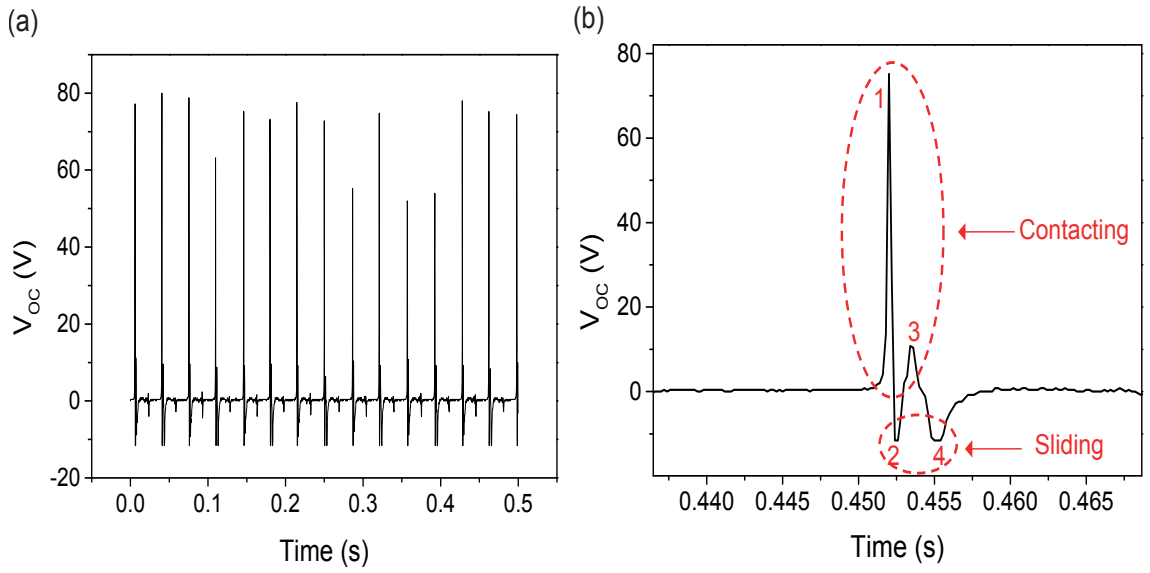

FIGURE 5.16: (a) Example of voltage peaks obtained when using our device with two Nylon plates and a PTFE plate, using a water flow of 30 L/min. (b) Magnification of a peak voltage and identification of respective processes involved.

The full cycle process involves the in-plane contact-sliding mode and the separation-contact mode in the vertical direction and a pair of alternating voltages is expected: one sharper but narrower peak corresponding to the vertical charge contact and one lower-magnitude but

wider peak corresponding to the in-plane charge separation. In Fig. 5.16(a) we illustrate one example of voltage peaks obtained for a device constituted by two Nylon plates and one PTFE plate, using a water flow of 30 L/min. In this example, we can see that each voltage peak is constituted by a peak that results from the contact process and a reverse peak (smaller) resulting from sliding process.

However, when we magnificate a voltage peak, we observe that there are in fact two peaks that result from the contact process and two peaks from the sliding process [Fig. 5.16(b)]. Initially, the first and second peak result from the contacting and sliding processes of a high contact surface between the plates. However, there are certain regions of the surfaces of the triboelectric materials that come into contact only after the above mentioned processes. This leads to a third and fourth peak resulting from the contacting and sliding processes as illustrated in Fig. 5.16(b). This suggests that the plates involved in the triboelectric process may have bends.

Chapter 6

Conclusions and Future Work

6.1 Conclusions

Triboelectric nanogenerators allow to capture green energy from the environment and the opportunity to harvest lower energy amplitudes. Enjoying natural mechanical energy from water streams, wind flows, material oscillations or bendings, it is possible to continuously feed electronic devices. These triboelectric NGs are conversion systems with high potential due to its simple and inexpensive manufacture and high power densities achievable.

In this project our main objective was to develop a triboelectric nanogenerator able to harvest energy from water motions. So, we demonstrated an innovative type of triboelectric nanogenerator for effectively harvesting water energy, especially for weak-water flows. The rotary TENG was designed to operate in three different triboelectric configurations. We verified that in all configurations, our device reached electrical output values higher for a water flow of 30 L/min.

For the first configuration, one plate for each material (Nylon and PTFE), the TENG produces an output voltage mean of $\sim$ 90.3 V and a mean short-circuit current of $\sim$ 79.6 μA, with a power density of $\sim$ 4.5 W/m^2. When the rotary TENG was two Nylon and one PTFE plates, $< V_{OC} >$ and mean short-circuit current was $\sim$ 69.6 V and $\sim$ 53.9 μA, respectively, and its maximum power density was $\sim$ 2.3 W/m^2. Lastly, with four Nylon and one PTFE plates,

$< V_{OC} >$ and $< I_{SC} >$ was $\sim$ 75.3 V and $\sim$ 77.7 μA, respectively, with a maximum power density of $\sim$ 4.1 W/m^2.

However, we determined that the structure constituted by four brackets, i.e., four Nylon plates and one PTFE plate, allows to obtain a better device performance, with a power per second $\sim$ 153.7 mW/s and power per cycle $\sim$ 11.0 mW/cycle for the water flow of 30 L/min.

Finally, to improve the performance of this device, we replaced the PTFE film by a textured PDMS one. We modified the surface of the PDMS using a Si mold (with micro-pyramid patterns) and an aluminum foil with ordered hexagonal arrays of nano-pits at its surface, and tested their influence when compared to the non-structured surface. Our results showed a 2$\times$ increase of the output voltage for the textured PDMS plate.

The electricity generation process of our rotary TENG results from the hybridization of contact-sliding-separation-contact processes. Through the distinct relationship between the water flow and the characteristics of the generated electrical output, our rotary TENG can be used as a self-powered water flow sensor. The future development and optimization of this device can open the possibility for applying it as sensor to monitor water supply systems, working and sending data using the energy produced by water movement in plumbing.

6.2 Future Work

As future work we want to optimize the copper brush that makes the electrical contact with the shaft in our TENG, because it was found to oxidize over time. Also, the fact that we use aluminum tape as electrode, may influence the electrical results. This is because this tape has a larger resistance than desirable and only in certain regions does electrostatic induction occurs. We want to replace this aluminum tape by another conductive material without glue.

In the future it is also necessary to study the dimensions of micro- and nanostructures on the surfaces of triboelectric materials, as well as to optimize the production methods of micro- and nanostructures discussed throughout this project. We want to optimize the triboelectric system response to external stimulus through a systematic study of the morphology and structure of TENG.

Another future work is to increase the sensitivity of our device for lower water flows. Additionally, we aim to miniaturize our rotary TENG to apply this technology in the microfluidics field.

Furthermore, we aim to apply this technology for application as a sensor to monitor water supply systems that can work, and send data using water movement in plumbing. Finally, we want to construct a hybrid rotary TENG by incorporating other types of energy harvesters, such as piezoelectric nanogenerators.

Bibliography

[1] Z. H. Lin, G. Cheng, S. Lee, K. C. Pradel, and Z. L. Wang, "Harvesting Water Drop Energy by a Sequential Contact-Electrification and Electrostatic-Induction Process," *Advanced Materials*, vol. 26, no. 27, pp. 4690–4696, 2014.

[2] S. Wang, L. Lin, and Z. L. Wang, "Nanoscale-Triboelectric-Effect Enabled Energy Conversion for Sustainable Powering of Portable Electronics," *Nano Letters*, vol. 12, no. 12, pp. 6339–46, 2012.

[3] Z. L. Wang, "Triboelectric Nanogenerators as New Energy Technology for Self-Powered Systems and as Active Mechanical and Chemical Sensors," *ACS Nano*, vol. 7, no. 11, pp. 9533–9557, 2013.

[4] Y. Xie, S. Wang, S. Niu, L. Lin, Q. Jing, Y. Su, Z. Wu, and Z. L. Wang, "Multi-Layered Disk Triboelectric Nanogenerator for Harvesting Hydropower," *Nano Energy*, vol. 6, pp. 129–136, 2014.

[5] Y. Yang, G. Zhu, H. Zhang, J. Chen, X. Zhong, Z. H. Lin, Y. Su, P. Bai, X. Wen, and Z. L. Wang, "Triboelectric Nanogenerator for Harvesting Wind Energy and as Self-Powered Wind Vector Sensor System," *ACS Nano*, vol. 7, no. 10, pp. 9461–9468, 2013.

[6] G. Zhu, Y. Su, P. Bai, J. Chen, Q. Jing, W. Yang, and Z. L. Wang, "Harvesting Water Wave Energy by Asymmetric Screening of Electrostatic Charges on a Nanostructured Hydrophobic Thin-Film Surface," *ACS Nano*, vol. 8, no. 6, pp. 6031–6037, 2014.

[7] W. Tang, T. Jiang, F. R. Fan, A. F. Yu, C. Zhang, X. Cao, and Z. L. Wang, "Liquid-Metal Electrode for High-Performance Triboelectric Nanogenerator at an Instantaneous Energy

Conversion Efficiency of 70.6%," *Advanced Functional Materials*, vol. 25, no. 24, pp. 3718–3725, June 2015.

[8] H. R. Zhu, W. Tang, C. Z. Gao, Y. Han, T. Li, X. Cao, and Z. L. Wang, "Self-powered metal surface anti-corrosion protection using energy harvested from rain drops and wind," *Nano Energy*, vol. 14, pp. 193–200, May 2015.

[9] "Hydroelectric Energy (Power) Pros and Cons." `http://www.renewablegreenenergypower.com/hydroelectric-energy-power-pros-and-cons/`. Accessed in 13th January 2015.

[10] "Wind Energy Pros and Cons." `http://energyinformative.org/wind-energy-pros-and-cons/`. Accessed in 10th January 2015.

[11] Y. Yang, W. Guo, K. C. Pradel, G. Zhu, Y. Zhou, Y. Zhang, Y. Hu, L. Lin, and Z. L. Wang, "Pyroelectric Nanogenerators for Harvesting Thermoelectric Energy," *Nano Letters*, vol. 12, no. 6, pp. 2833–2838, 2012.

[12] S. N. Cha, J. S. Seo, S. M. Kim, H. J. Kim, Y. J. Park, S. W. Kim, and J. M. Kim, "Sound-driven Piezoelectric Nanowire-Based Nanogenerators," *Advanced Materials*, vol. 22, no. 42, pp. 4726–4730, 2010.

[13] G. Cheng, Z. H. Lin, Z. L. Du, and Z. L. Wang, "Simultaneously Harvesting Electrostatic and Mechanical Energies from Flowing Water by a Hybridized Triboelectric Nanogenerator," *ACS Nano*, vol. 8, no. 2, pp. 1932–1939, 2014.

[14] Z. L. Wang and J. Song, "Piezoelectric Nanogenerators Based on Zinc Oxide Nanowire Arrays.," *Science (New York, N.Y.)*, vol. 312, no. 5771, pp. 242–246, 2006.

[15] X. Wang, "Piezoelectric Nanogenerators—Harvesting Ambient Mechanical Energy at the Nanometer Scale," *Nano Energy*, vol. 1, no. 1, pp. 13–24, January 2012.

[16] P.-K. Yang, Z.-H. Lin, K. C. Pradel, L. Lin, X. Li, X. Wen, J.-H. He, and Z. L. Wang, "Paper-Based Origami Triboelectric Nanogenerators and Self-Powered Pressure Sensors," *ACS Nano*, vol. 9, no. 1, pp. 901–907, January 2015.

[17] H. Guo, J. Chen, M.-H. Yeh, X. Fan, Z. Wen, Z. Li, C. Hu, and Z. L. Wang, "An Ultrarobust High-Performance Triboelectric Nanogenerator Based on Charge Replenishment," *ACS Nano*, vol. 9, no. 5, pp. 5577–5584, May 2015.

[18] G. Zhu, B. Peng, J. Chen, Q. Jing, and Z. L. Wang, "Triboelectric nanogenerators as a new energy technology: From fundamentals, devices, to applications," *Nano Energy*, vol. 14, pp. 126 – 138, 2015.

[19] D. M. Gooding and G. K. Kaufman, "Tribocharging and the Triboelectric Series," *Encyclopedia of Inorganic and Bioinorganic Chemistry*, pp. 1–9, 2014.

[20] F. Galembeck, T. A. L. Burgo, L. B. S. Balestrin, R. F. Gouveia, C. A. Silva, and A. Galembeck, "Friction, tribochemistry and triboelectricity: Recent progress and perspectives," *RSC Advances*, vol. 4, pp. 64280–64298, 2014.

[21] B. Bhushan, *Introduction to Tribology, Second Edition*. Wiley, New York, Chapter 1, 2013.

[22] P. L. Menezes, C. J. Reeves, and M. R. Lovell, "Tribology for Scientists and Engineers: From Basics to Advanced Concepts ," *Springer*, pp. 295–340, 2013.

[23] J. Lowell and A. C. Rose-Innes, "Contact Electrification," *Advances in Physics*, vol. 29, no. 6, pp. 947–1023, July 1980.

[24] Z. L. Wang, J. Chen, and L. Lin, "Progress in Triboelectric Nanogenerators as a New Energy Technology and Self-Powered Sensors," *Energy & Environmental Science*, vol. 8, no. 8, pp. 2250–2282, 2015.

[25] V. Nguyen and R. Yang, "Effect of Humidity and Pressure on the Triboelectric Nanogenerator," *Nano Energy*, vol. 2, no. 5, pp. 604–608, September 2013.

[26] L. S. McCarty and G. M. Whitesides, "Electrostatic Charging Due to Separation of Ions at Interfaces: Contact Electrification of Ionic Electrets," *Angewandte Chemie - International Edition*, vol. 47, no. 12, pp. 2188–2207, 2008.

[27] B. Yang, H. Liu, J. Liu, and C. Lee, *Micro and Nano Energy Harvesting Technologies*. Artech House, 2014.

[28] F. R. Fan, Z. Q. Tian, and Z. Lin Wang, "Flexible Triboelectric Generator," *Nano Energy*, vol. 1, no. 2, pp. 328–334, 2012.

[29] Z. H. Lin, G. Cheng, W. Wu, K. C. Pradel, and Z. L. Wang, "Dual-Mode Triboelectric Nanogenerator for Harvesting Water Energy and as a Self-Powered Ethanol Nanosensor," *ACS Nano*, vol. 8, no. 6, pp. 6440–6448, 2014.

[30] S. Niu and Z. L. Wang, "Theoretical Systems of Triboelectric Nanogenerators," *Nano Energy*, vol. 14, pp. 161–192, 2015.

[31] S. Niu, Y. S. Zhou, S. Wang, Y. Liu, L. Lin, Y. Bando, and Z. L. Wang, "Simulation Method for Optimizing the Performance of an Integrated Triboelectric Nanogenerator Energy Harvesting System," *Nano Energy*, vol. 8, pp. 150–156, September 2014.

[32] S. Wang, L. Lin, and Z. Lin, "Triboelectric Nanogenerators as Self-Powered Active Sensors," *Nano Energy*, vol. 11, pp. 436–462, 2015.

[33] Z. L. Wang, "Triboelectric Nanogenerators as New Energy Technology and Self-Powered Sensors - Principles, Problems and Perspectives," *Faraday Discussions*, vol. 176, pp. 447–458, 2014.

[34] S. Li, S. Wang, Y. Zi, Z. Wen, L. Lin, G. Zhang, and Z. L. Wang, "Largely Improving the Robustness and Lifetime of Triboelectric Nanogenerators Through Automatic Transition Between Contact and Noncontact Working States," *ACS Nano*, vol. 9, no. 7, pp. 7479–7487, July 2015.

[35] F. Yi, L. Lin, S. Niu, P. K. Yang, Z. Wang, J. Chen, Y. Zhou, Y. Zi, J. Wang, Q. Liao, Y. Zhang, and Z. L. Wang, "Stretchable-Rubber-Based Triboelectric Nanogenerator and Its Application as Self-Powered Body Motion Sensors," *Advanced Functional Materials*, vol. 25, no. 24, pp. 3688–3696, June 2015.

[36] Y. Hu, J. Yang, Q. Jing, S. Niu, W. Wu, and Z. L. Wang, "Triboelectric Nanogenerator Built on Suspended 3D Spiral Structure as Vibration and Positioning Sensor and Wave Energy Harvester," *ACS Nano*, vol. 7, no. 11, pp. 10424–10432, 2013.

[37] L. Lin, Y. Xie, S. Niu, S. Wang, P.-K. Yang, and Z. L. Wang, "Robust Triboelectric Nanogenerator Based on Rolling Electrification and Electrostatic Induction at an Instantaneous

Energy Conversion Efficiency of Similar to 55%," *ACS Nano*, vol. 9, no. 1, pp. 922–930, January 2015.

[38] S. Niu, Y. Liu, S. Wang, L. Lin, Y. S. Zhou, Y. Hu, and Z. L. Wang, "Theoretical Investigation and Structural Optimization of Single-Electrode Triboelectric Nanogenerators," *Advanced Functional Materials*, vol. 24, no. 22, pp. 3332–3340, June 2014.

[39] S. Wang, S. Niu, J. Yang, L. Lin, and Z. L. Wang, "Quantitative Measurements of Vibration Amplitude Using a Contact-Mode Freestanding Triboelectric Nanogenerator," *ACS Nano*, vol. 8, no. 12, pp. 12004–12013, December 2014.

[40] S. Niu, Y. Liu, X. Chen, S. Wang, Y. S. Zhou, L. Lin, Y. Xie, and Z. L. Wang, "Theory of freestanding triboelectric-layer-based nanogenerators," *Nano Energy*, vol. 12, pp. 760 – 774, 2015.

[41] S.-H. Shin, Y. H. Kwon, Y.-H. Kim, J.-Y. Jung, M. H. Lee, and J. Nah, "Triboelectric Charging Sequence Induced by Surface Functionalization as a Method To Fabricate High Performance Triboelectric Generators," *ACS Nano*, vol. 9, no. 4, pp. 4621–4627, April, 2015.

[42] C. Zhang, W. Tang, C. Han, F. Fan, and Z. L. Wang, "Theoretical Comparison, Equivalent Transformation, and Conjunction Operations of Electromagnetic Induction Generator and Triboelectric Nanogenerator for Harvesting Mechanical Energy," *Advanced Materials*, vol. 26, no. 22, pp. 3580–3591, June 2014.

[43] Z. H. Lin, G. Zhu, Y. S. Zhou, Y. Yang, P. Bai, J. Chen, and Z. L. Wang, "A Self-Powered Triboelectric Nanosensor for Mercury Ion Detection," *Angewandte Chemie - International Edition*, vol. 52, no. 19, pp. 5065–5069, 2013.

[44] P. Bai, G. Zhu, Q. Jing, J. Yang, J. Chen, Y. Su, J. Ma, G. Zhang, and Z. L. Wang, "Membrane-Based Self-Powered Triboelectric Sensors for Pressure Change Detection and its Uses in Security Surveillance and Healthcare Monitoring," *Advanced Functional Materials*, vol. 24, no. 37, pp. 5807–5813, October 2014.

[45] X.-S. Zhang, M.-D. Han, B. Meng, and H.-X. Zhang, "High Performance Triboelectric Nanogenerators Based on Large-Scale Mass-Fabrication Technologies," *Nano Energy*, vol. 11, pp. 304–322, January 2015.

[46] C. K. Jeong, K. M. Baek, S. Niu, T. W. Nam, Y. H. Hur, D. Y. Park, G.-T. Hwang, M. Byun, Z. L. Wang, Y. S. Jung, and K. J. Lee, "Topographically-Designed Triboelectric Nanogenerator via Block Copolymer Self-Assembly," *Nano Letters*, vol. 14, no. 12, pp. 7031–7038, 2014.

[47] F. R. Fan, L. Lin, G. Zhu, W. Wu, R. Zhang, and Z. L. Wang, "Transparent Triboelectric Nanogenerators and Self-Powered Pressure Sensors Based on Micropatterned Plastic Films," *Nano Letters*, vol. 12, no. 6, pp. 3109–3114, 2012.

[48] X. Wen, W. Yang, Q. Jing, and Z. L. Wang, "Harvesting Broadband Kinetic Impact Energy from Mechanical Triggering/Vibration and Water Waves," *ACS Nano*, vol. 8, no. 7, pp. 7405–7412, 2014.

[49] Q. Jing, G. Zhu, P. Bai, Y. Xie, J. Chen, R. P. S. Han, and Z. L. Wang, "Case-Encapsulated Triboelectric Nanogenerator for Harvesting Energy from Reciprocating Sliding Motion," *ACS Nano*, vol. 8, no. 4, pp. 3836–3842, April 2014.

[50] S. Wang, X. Mu, Y. Yang, C. Sun, A. Y. Gu, and Z. L. Wang, "Flow-Driven Triboelectric Generator for Directly Powering a Wireless Sensor Node," *Advanced Materials*, 2015.

[51] J. Chen, J. Yang, Z. Li, X. Fan, Y. Zi, Q. Jing, H. Guo, Z. Wen, K. C. Pradel, S. Niu, and Z. L. Wang, "Networks of Triboelectric Nanogenerators for Harvesting Water Wave Energy: A Potential Approach toward Blue Energy," *ACS Nano*, vol. 9, no. 3, pp. 3324–3331, March 2015.

[52] Y. Zi, L. Lin, J. Wang, S. Wang, J. Chen, X. Fan, P.-K. Yang, F. Yi, and Z. L. Wang, "Triboelectric-Pyroelectric-Piezoelectric Hybrid Cell for High-Efficiency Energy-Harvesting and Self-Powered Sensing," *Advanced Materials*, vol. 27, no. 14, pp. 2340–2347, April 2015.

[53] Dow Corning, "Sylgard 182 Silicone Elastomer Kit." `http://www.dowcorning.com/DataFiles/090276fe8018f8ee.pdf`. Accessed in 10th March 2015.

[54] F. R. Fan, J. Luo, W. Tang, C. Li, C. Zhang, Z. Tian, and Z. L. Wang, "Highly Transparent and Flexible Triboelectric Nanogenerators: Performance Improvements and Fundamental Mechanisms," *Journal of Materials Chemistry A*, vol. 2, no. 33, pp. 13219–13225, September 2014.

[55] S. Lee, W. Ko, Y. Oh, J. Lee, G. Baek, Y. Lee, J. Sohn, S. Cha, J. Kim, J. Park, and J. Hong, "Triboelectric Energy Harvester Based on Wearable Textile Platforms Employing Various Surface Morphologies," *Nano Energy*, vol. 12, pp. 410–418, March 2015.

[56] L. E. Scriven, "Physics and Applications of Dip Coating and Spin Coating," 1988.

[57] O. Jessensky, F. Muller, and U. Gosele, "Self-Organized Formation of Hexagonal Pore Arrays in Anodic Alumina," *Applied Physics Letters*, vol. 72, no. 10, pp. 1173–1175, 1998.

[58] Laboratory of Self-Organized Nano Fabrication, "Laboratory Documents - Electropolishing." 2012.

[59] M. J. P. Proença, "Magnetism at the Nanoscale : Nanoparticles, Nanowires, Nanotubes and their Ordered Arrays." PhD thesis, Faculty of Sciences of the University of Porto, 2012.

[60] Tektronix, "Digital Storage Oscilloscopes- TDS1000C-EDU Series Data Sheet." Tektronix, 2013.

[61] National Instruments. NI GPIB-USB-HS, 2012.

[62] Stanford Research Systems, "User Manual SR560 — Low-noise preamplifier." Stanford Research Systems, 2013.

[63] ARDUINO, "Arduino UNO." `https://www.arduino.cc/en/Main/arduinoBoardUno`. Accessed in 29th April 2015.